Fall 2018

Characterization and tailoring of powder used in additive manufacturing and plasma spheroidization

Caitlin S. Kriewall

Department:

CHARACTERIZATION AND TAILORING OF POWDER USED IN ADDITIVE MANUFACTURING AND PLASMA SPHEROIDIZATION

by

CAITLIN SHEA KRIEWALL

A THESIS

Presented to the Faculty of the Graduate School of the

MISSOURI UNIVERSITY OF SCIENCE AND TECHNOLOGY

In Partial Fulfillment of the Requirements for the Degree

MASTER OF SCIENCE IN MATERIALS SCIENCE AND ENGINEERING

2018

Approved by:

Joseph W. Newkirk
Frank Liou
Laura Bartlett

PUBLICATION THESIS OPTION

This thesis consists of 3 papers that have been published or will be submitted for publication. The papers contained in this paper are as follows:

Paper I: Pages 13-35 “Investigation of heat-affected 304L SS powder and its effect on built parts in selective laser melting” was published in the Solid Freeform Fabrication conference proceedings pages 625-639 in 2016.

Paper II: Pages 36-54 “Effects of area fraction and part spacing on degradation of 304L stainless steel powder in selective laser melting” was published in the Solid Freeform Fabrication conference proceedings pages 277-288 in 2017

Paper III: Pages 55-73 “Plasma spheroidization of Vitreloy 106A Powder” has been prepared for submission to Journal of Materials Processing Technology.

ABSTRACT

There are many processes that use metal powder as the starting material for the production of parts. With the growth of these manufacturing techniques, more critical part applications are being considered. In order to fully understand the process and create consistent parts, powder properties need to be well understood. Selective laser melting (SLM) is a powder bed-based additive manufacturing process. During processing, heat-affected powders are generated and can deposit within the build area. The current work investigated the characterization of heat-affected 304L stainless steel powder using techniques such as scanning electron microscopy, x-ray diffraction and x-ray photoelectron spectroscopy to detect differences in the heat-affected powder and to determine the best way to detect them. This heat-affected powder can also have an influence on the amount of times that the powder can be reused. A methodology was proposed where a fast, miniature powder recycling study was conducted. Area fractions and part spacing where deterioration of powder was observed can then be used to design a more in depth recycling study. The use of SLM for processing of more exotic materials such as metallic glasses was also of interest. However, the acquisition of powder forms of these materials that are suitable for processing via SLM is difficult and expensive. The work in this thesis aimed to use plasma spheroidization to tailor inert ground, angular Vitreloy 106A metallic glass powder and spheroidize it so that it was suitable for use in additive manufacturing processes. Several powder characterization techniques were used to evaluate the success of the process including x-ray diffraction, differential scanning calorimetry and Raman spectroscopy.

ACKNOWLEDGMENTS

I would first like to thank my advisor Dr. Joseph Newkirk. Dr. Newkirk has helped my tremendously not only with my academic grown but also my personal development over the years. He has consistently been a wonderful mentor and I greatly appreciate the effort he put towards my education. Besides my advisor I would also like to thank my committee members Dr. Frank Liou and Dr. Laura Bartlett for their input.

The members of the various research groups and instrument staff I have worked in were all great. I would like to specifically thank Sreekar Karnati and Austin Sutton for their continual input on my research. The instrument specialists including Dr. Jessica TerBush, Dr. Clarissa Wisner, Dr. Jingjing Qing and Dr. Eric Bohannan were consistently knowledgeable and kind and I appreciate their input.

I would like to thank Honeywell FM&T for funding this work and Materion for providing materials.

I would like to thank my wonderful family, my mother Cheryl, my father Kevin, and my sister Kalise for their support and generosity. Finally, I would like to thank my amazing husband Dr. Mohsen Beyramali Kivy for always being there for me and believing in me.

TABLE OF CONTENTS

Page

SECTION

LIST OF ILLUSTRATIONS

LIST OF TABLES

1. INTRODUCTION

1.1. STAINLESS STEEL

Steels are iron-carbon alloys that have seen extensive use because they are inexpensive and have excellent mechanical properties [1]. Although steels have many advantageous properties, the degradation of the material via corrosion was a major downfall for critical uses. Research dating back to the 19th century was seeking ferrous alloys that had improved corrosion resistance [2]. Nonferrous materials offered good corrosion resistance however the inferior mechanical properties and added expense associated with their use were undesirable [3]. Many independent researchers in the early 20th century discovered alloys that are now considered stainless steels. Philip Monnartz is credited with being the first person to understanding the corrosion resistance associated with stainless steel. In his research published in 1908, Monnartz details several characteristics of stainless steels including that the drop in corrosion rate for iron alloys at 12% chromium was due to passivation and carbon in the alloy leads to the formation of chromium carbides that prevent passivation, a phenomenon called sensitization [4]. Passivation in stainless steels involves the production of a very thin layer of chromium-rich oxide that protects the surface of the material from oxidation [5]. The discovery of stainless steel, “the miracle metal”, was a major metallurgical achievement. In the 1970s, techniques were developed that enabled the decarburization of stainless steel melts without considerable loss of chromium which transformed the production of stainless steel by increasing the efficiency in production and reducing the overall cost [3]. Stainless steels have seen widespread use in industries including petroleum engineering

[6], automobile industries [7], construction [8], food industries [9], in decorative pieces and more.

Stainless steel is defined as a steel alloy with at least 12 wt% chromium. Stainless steels are categorized according to their microstructure where there are austenitic (face-centered cubic, fcc), ferritic (body-centered cubic, bcc), martensitic (body-centered tetragonal), and duplex (mixed) [10]. Research in the welding of stainless steels determined that the microstructure could be controlled by adjustment of the alloying elements and can be predicted by what is called the chrome nickel equivalent [11]. Chromium has bcc crystal structure and stabilized ferrite while nickel has an fcc crystal structure and stabilized austenite. While chromium and nickel provide the largest impact on the chromium nickel equivalent due to their high concentration in stainless steel, other common alloying elements have an effect on the structure as well. Carbon and manganese are like nickel in that they stabilize austenite while molybdenum and niobium stabilize ferrite like chromium [12]. Diagrams, such as the Shaeffler diagram [11] and several welding research council modifications [12,13], graph the nickel equivalent vs the chromium equivalent and can make predictions of whether the microstructure will be purely austenite, ferrite, martensite or a mixture of phases. These diagrams have also been used to predict the amount of ferrite retained in weld chemistries that contain mixed microstructure of austenite and ferrite.

304L stainless steel is a common austenitic stainless steel. The L in 304L stands for low carbon which is necessary to reduce sensitization as previously mentioned [5,14]. The chemistry requirement as well as typical mechanical property requirements for 304L stainless steel are shown in Table 1.1 [15]. 304L stainless steel exists in an austenite-

ferrite region of the welding research council constitution diagram where the percentage of ferrite can vary from 2-8wt.% [12]. 304L stainless steel is popular due to the excellent corrosion resistance and mechanical properties that the alloy exhibits. 304L stainless steel is also readily weldable making them a good candidate for processing though newer techniques such as additive manufacturing (AM) [14].

Table 1.1: Chemical and tensile requirements for 304L stainless steel.

Chemistry	Element	C	Cr	Fe	Mn	N	Ni	P	S	Si
Requirement	Wt. %	≤ 0.030	17.5-19.5	Bal.	2.00	0.10	8.0-12.0	0.045	0.030	0.75
Tensile Test	Yield Strength			Tensile Strength			Elongation			
Requirements	170 MPa			485 MPa			40%			

1.2. BULK METALLIC GLASSES

Metallic alloys generally have cubic crystalline structure [1]. Metallic glasses, on the other hand, are multicomponent metal alloys that possess no long-range order in their structure and are therefore amorphous. These materials have several unique properties including their high strengths, high fracture toughness and good corrosion and wear resistance due to their lack of grain boundaries and dislocations [16,17]. This makes these alloys suitable for a wide range of applications including tool materials, cutting materials and hydrogen storage materials [18]. Metallic glasses were first described by Duwez *et al.* in 1960 for $Au_{75}Si_{25}$ alloy where cooling rates of 10^5-10^6 K/s were achieved in their rapid quenching process [19]. Continuous casting processes enabled more research into

metallic glasses to be possible in the 1970s and 1980s [20]. The early years of metallic glass exploration also showed that these alloys exhibited glass transitions such as those seen in polymers. The ratio between the glass transition temperature (T_g) and the liquidus temperature ™, known as the reduced glass temperature ($T_{rg} = T_g/T_m$), became an important parameter in assessing an alloys ability to form a glass [20]. However, in order to make parts thicker than ribbons and sheets, processes with higher cooling rates and/or alloys with lower critical cooling rates had to be utilized.

Metallic glasses are considered ‘bulk’ once the amorphous microstructure is present in a 1 mm diameter sample [20]. While the first bulk metallic glass (BMG) was discovered in 1974, a time of major development of metallic glasses was in the 1990s and early 2000s where several different metallic glass forming alloy systems were discovered [17, 18, 20]. These BMG alloys have compositions that land them near deep eutectic regions where low melting points and high viscosities are reported [21]. Through this period of development of BMGs several different manufacturing methods suitable for processing of metallic glass parts were realized including suction-casting, arc-melting and copper mold casting [22]. The production of metallic glass powder was also being explored for use in other manufacturing processes. The use of metallic glass powder has several potential production methods including extrusion, rolling, cold spray and AM [21,23–27]. AM applications specifically require spherical powders in order to have good flowability. The work in this thesis looked at improving the sphericity and flowability of inert ground Vitreloy 106A BMG powder. Vitreloy 106A is a Zr-based BMG with the

following chemistry: $Zr_{58.5}Cu_{15.6}Ni_{12.8}Al_{10.3}Nb_{2.8}$ [28]. This BMG has excellent glass forming ability with a critical cooling rate of 1.75 K/s [24].

1.3. ADDITIVE MANUFACTURING

Rapid prototyping was the name given to techniques that were used to manufacture small models of parts in a timely manner [29]. Over time the use of this technology to build full-scale parts has been realized. Additive manufacturing (AM) is the name given to a wide array of manufacturing techniques where parts are built in an additive fashion, i.e. layer-by-layer, as opposed to the traditional manufacturing methods that use subtractive methods [30]. AM offers several advantages such as the ability to create complex geometries that cannot be machined, the simplification of parts, and the reduction of waste material. Parts made from polymers, ceramics, glasses and metals can be produced using AM. The growth of AM has attracted the interest of researchers and industries alike. AM is now being considered as a viable manufacturing method for industries that require more critical applications such as aerospace [31]. All aspects of the process are under more intense study as complete understanding will be required to develop the necessary standards for industrial use of AM.

With regards to metals, AM techniques have expanded to accommodate starting materials in the form of metal wire, foil and powder [29, 30]. Powders used in the AM process are desired to be spherical and have a relatively narrow particle size distribution. Selective laser melting (SLM) is an AM technique that utilizes a powder bed to build parts. As with all AM technology the first step of SLM is to create a CAD model of the desired final part and load this onto the machine [31]. In SLM a layer of powder is spread

over a build plate and the laser is used to consolidate powder in predetermined areas. Once the layer is finished the build plate is incremented down and the process is repeated until final part geometry is reached. Argon gas cross-flow in the build area is commonly used to attempt to remove all undesirable by-products of the laser interacting with the powder bed [32]. SLM has many process parameters that can be controlled however laser power, laser scan speed, hatch spacing and layer thickness generally have the largest impact on resulting parts [33]. SLM produces parts with superior dimensional accuracy and surface finish when compared to other AM methods such as blown-powder based methods [34]. Extensive research has been completed in attempts to understand all aspects of the process. One such aspect is powder usage and how the powder changes once it has been through the process.

When studying changes to powder that occur during the SLM process, modeling work in the literature provides a good descriptions of what occurs, while extensive powder characterization is needed to fully describe the process. When the laser interacts with the powder bed, vaporization of small particles and volatile elements occurs. This vaporization leads to two common types of heat-affected powders that are (1) laser spatter and (2) condensate. Laser spatter particles are formed when vaporized gases push molten material out of the melt pool [35–37]. These particles then solidify and are either deposited in the build chamber or pushed to the side or through the filtration system by the cross-flow of gas. These spatter particles generally have different surface and bulk chemistry conditions compared to the starting powder [24,27]. Laser spatter particles are generally referred to as being larger particles that contribute to the coarsening of particle size distributions with powder use. Laser spatter particles can, however, have sizes

similar to those of the starting powder [38]. Condensate powder forms when vaporized material rapidly cools and condenses as very fine particles [39, 40]. This condensate powder can interact with the laser beam causing defocusing which has a negative impact on part properties [36, 37, 39–41]. The aim of the work in this thesis was to characterize the heat-affected powder that was generated during SLM processing and determine whether its presence could be tied to any adverse effect on tensile properties, density and surface roughness of the parts.

For SLM builds, usually between 10%-50% of the build plate is used to build parts, where a large portion of the input powder has no contact with the laser. The ability to reuse powder is of great importance when considering the economic and environmental impacts. Currently between 5-46% of the cost of SLM is associated with material costs [42]. Powder characteristics and their effect on part properties must be understood before reuse of powder can be implemented. Metal powder recycling studies are currently sparse in literature, but materials such as Ti64 [43], Inconel 718 [44], 17-4 PH stainless steel and CoCr [45] have been studied. All of these studies were carried out on SLM machines apart from the Tang *et al.* study of Ti64 which used an electron beam melting (EBM) system. EBM systems are similar to SLM except an electron beam is used instead of a laser to melt powder particles. General findings include coarsening of powder with reuse, improved flowability with reuse and, more importantly, Ti64 and Inconel 718 powders could be reused up to 14 and 21 times respectively with no adverse effects [43, 44]. One important note is that these studies did not present a methodology behind their build design; they simply presented a certain build and indicated that it was repeated through multiple iterations. Remember that heat-affected powder is generated

when the laser interacts with the powder bed and this heat-affected powder has been shown to have an effect on part properties. Thus, the amount of the build area that was used to make parts is important as it is directly related to the amount of heat-affected powder generated. The work in this thesis aims to establish a simple and quick approach to design a powder recycling study for the SLM process. This methodology could be used to perform a preliminary study where build areas that are known to influence powder properties can be identified and used for more in depth recycling studies spanning several iterations.

1.4. INDUCTIVELY COUPLED PLASMA

Plasma, commonly referred to as the fourth state of matter, is simply an ionized gas [46]. At high enough temperatures, the atoms and molecules that make up a gas are moving so fast that when they collide, electrons are knocked off, ionizing the atoms and molecules [47]. Plasmas have unique properties such as their ability to conduct electricity and their interactions with magnetic fields. There are several different types of plasmas but one of the more common types of high-temperature plasmas is an inductively coupled plasma (ICP) [48]. A typical ICP source, i.e. torch, consists of 3 concentric quartz tubes used to contain the flowing gasses (typically argon and hydrogen), a Tesla coil used to start the ionization and a water cooled induction coil. A radio frequency is passed through the induction coil which creates a rapidly oscillating magnetic field. The Tesla coil is use to induce the initial ionization of the argon gas. The interaction of the ions with the magnetic field leads to more collisions and therefore more ionization. The high speeds attained by the atoms, ions and electrons yields further ionization and a substantial

temperature rise, effectively creating the high-temperature plasma [48]. Argon is commonly used as the plasma forming gas and addition of hydrogen improves the thermal conductivity and consequently improves the energy transfer from the plasma to the material of study [49]. Temperatures of argon ICPs are generally between 6,000 and 10,000 K but can be higher [50].

ICPs are commonly used to dissociate elements for analytical chemistry including atomic emission spectroscopy [51, 52] and mass spectrometry [53–55]. However, other applications of the technology are still being determined. One such application is the use of ICPs to spheroidize powder particles [56]. The application of ICP to powders offers several advantages including increases in flowability/sphericity, density and even purification of contaminated particles [576]. The ease of use of commercial plasma systems have enabled widespread use. Companies such as Tekna are creating plasma systems ranging from those for research and development to large scale systems intended for industrial production [57]. In these systems the powder is fed through the plasma using argon as the carrier gas. When the powder passes through the plasma, the high temperatures result in melting of the surface layers of the powder particles. The powder particles are then cooled and form a spherical shape due to spheres having a lower surface energy. The high temperatures achieved by the plasma enables the spheroidization of a wide variety of materials including 316L stainless steel [58], titanium [59], titanium carbide [60], tungsten and molybdenum [61] just to name a few.

The research discussed in this thesis involved the use of a Tekna inductively coupled plasma spheroidization system to spheroidize Vitreloy 106A metallic glass inert ground powder. Two main issues were associated with the processing of Vitreloy 106A.

First, Vitreloy 106A has a relatively low melting point at around 866°C [62]. This low melting point could lead to complete vaporization of material or the powder could still be in a molten state when hitting the walls of the reaction chamber, resulting in a coating instead of the desired powder particles. Also, Vitreloy 106A is a Zr-based metallic glass. Selective vaporization is always a possibility when processing alloys through plasma and therefore the chemistry of the resulting powder can differ from the starting material. More importantly for the case of Vitreloy 106A, pure zirconium powder could be created during this process and a concentrated amount could be produced. In order to reduce the risks associated with this process, both a low plasma power and a passivation procedure were executed.

2. RESEARCH OBJECTIVES AND IMPACT

The overall goal of this research was to use powder characterization methods to enhance the understanding of powder degradation in the SLM process and to tailor powder for use in AM. 304L SS powder was used to build parts via SLM and powder characterization was used to assess powder degradation. Tailoring of inert ground Vitreloy 106A powder to improve powder properties through plasma spheroidization was also explored. The specific objectives were:

- Objective 1: Determine characterization techniques to detect differences between new and used 304L SS powder
    - Used SLM to build parts where different build geometries were utilized to generate different amounts of heat-affected powder
    - Used several powder characterization techniques to determine which ones were suitable to detect differences in the used and starting powder
    - Determine whether property differences were observed
- Objective 2: Use knowledge of 304L powder degradation to create build design methodology
    - Completed multiple builds with different area fraction and part spacings while recycling powder through 3 iterations
    - Determined what powder differences occurred and whether property differences were present
    - Used the information to give a recommendation of build requirements for a longer, more in depth recycling study

- Objective 3: Tailor Vitreloy 106A inert ground powder via plasma spheroidization and assess success with powder characterization
    - Used TekSphero-15 plasma spheroidization to tailor inert ground Vitreloy 106A powder.
    - Evaluated the success of the plasma processing via powder characterization

The results of this research outline the necessary characterization to detect 304L stainless steel that has been through the SLM process. This information was then applied to the recyclability of 304L stainless steel where a methodology to design builds for a larger recycling study was developed. Finally, several powder characterization methods were utilized to evaluate the success of plasma spheroidization to tailor Vitreloy 106A inert ground powder for AM processes.

PAPER

I. INVESTIGATION OF HEAT-AFFECTED 304L SS POWDER AND ITS EFFECT ON BUILT PARTS IN SELECTIVE LASER MELTING

Caitlin S. Kriewall[1], Austin T. Sutton[2], Ming C. Leu[2], Joseph W. Newkirk[1], Ben Brown[2,3]

[1]Department of Materials Science and Engineering, Missouri University of Science and Technology, Rolla, MO 65409

[2]Department of Mechanical and Aerospace Engineering, Missouri University of Science and Technology, Rolla, MO 65409

[3]Department of Energy's Kansas City National Security Campus Managed by Honeywell FM&T, Kansas City, MO 64147

(*Solid Freeform Fabrication Symposium Proceedings*, 2016)

ABSTRACT

Selective laser melting (SLM) is a powder bed based additive manufacturing process in which a layer of powder is laid over the surface of a substrate and a laser with sufficient energy is employed to selectively melt particles and build a part layer by layer. During the SLM process, dark smoke was observed coming off of the powder bed surface where the laser is interacting with powder. This phenomenon resulted in heat-affected powder that was visibly different from the base powder. Since the concentration of the heat-affected powder differs throughout the build chamber as a result of the recirculating argon gas flow, powder samples from different regions were collected for analysis. The heat-affected powder samples were analyzed by scanning electron microscopy (SEM), x-

ray photoelectron spectroscopy (XPS), and x-ray diffraction (XRD) in order to distinguish differences between the heat-affected powder and the base 304L stainless steel powder. The influences of the heat-affected powder on the microstructure and tensile properties of parts built in different areas of the build chamber were also investigated.

1. INTRODUCTION

Additive Manufacturing (AM) is a class of layer-based techniques used primarily for the creation of parts with complex geometry that are otherwise impossible or impractical to create through conventional means [1]. This technology enables the direct translation of Computer-Aided Design (CAD) data into tangible parts thereby decreasing the amount of design limitations imposed by manufacturability constraints [2]. As the AM industry reaches a stage of maturity since its conception with stereolithography in 1987 [3], the goal of being able to produce functional components becomes a priority. Although there exist many process variants that each can be categorized by the state of the starting material [4], a search of the existing literature indicates that many of the successful attempts to produce functional AM components stem from using powder as the raw input material [5].

Among the available powder-based additive methods is the selective laser melting (SLM) process in which successive layers of powder are selectively bonded by a laser. Rather than sinter particles together by forming bridges or through the use of a binder as in selective laser sintering (SLS), the consolidation mechanism in SLM relies on the

melting of material to form dense parts in a single step with little to no post-processing. However, as with any new manufacturing process there exists a research and development phase aimed at exploiting the true potential of this technology in order to solve crucial issues influencing part quality. A significant amount of research in SLM is focused on the optimization of process parameters for specific materials to produce parts of acceptable quality [6–9]. Often, variables such as laser power, scanning speed, hatch spacing, and layer thickness are tuned until satisfaction with part properties is met. Other work is directed towards understanding the relationship between input material properties and part characteristics [5,10–17]. These studies observe not only the influences of morphological characteristics of powder particles on the parts that are built but also the ramifications of differing chemistry and powder reuse.

In order to understand the fundamentals of the SLM process, researchers have also focused on rigorous modeling of the melting process [18–21]. In these simulations, the interaction between the laser and the powder bed can be observed. It has been noticed that the melt pool is a complex environment with fluid flow driven by Marangoni convection as a consequence of steep thermal gradients. It is also evident that a certain amount of vaporization of volatile elements and potentially small particles takes place due to a high energy input. This vaporization leads to two types of heat-affected powder: laser spatter and condensate. Laser spatter is a direct result of the upsurge of vaporized gases through the melt pool causing molten material to be ejected as a result of melt pool instabilities [22–24]. Once ejected, solidification of the molten material occurs while in the chamber atmosphere where it is later deposited elsewhere into the powder bed. These particles have been proven to be chemically different from the base powder [22], and

could potentially alter the properties of the parts in which landed upon during the build process. The other form of heat-affected powder, condensate, forms as a result of the vaporized material above the melt pool rapidly condensing [25,26]. As such, the majority of these particles are small and responsible for sticking to the surfaces within the build chamber. However, due to their small size agglomeration can occur leading to the formation of larger particles [25] heavy enough to settle inside the powder bed. If not properly removed, condensate can also interact with the laser beam causing attenuation and scattering [23–27], both of which can have negative impacts on the part quality.

In order to mitigate the interference between the laser and condensate cloud, the recirculating gas flow across the build area is optimized to be uniform and high as possible without disturbing the powder in each layer. Ferrar et al. [26] modeled the build chamber as well as the inlet and outlet gas flow configurations for the SLM machine under consideration so that a CFD simulation could be run to visualize the flow across the powder bed. It was found that the flow field was inconsistent producing regions of high gas flow and relatively stagnant flow in others. The inlet manifold was then optimized to improve the uniformity of flow across the bed. Another study [25] observed the influence of a varying gas flow on the surface irregularities of built parts in addition to the formation of material defects in regards to pores. The results showed that a reduced gas flow rate caused more interaction between the laser and the condensate cloud thereby increasing porosity, top surface roughness, and the overall width of the laser scan. However, material properties were not quantified so as to observe the degree of influence of the reduced gas recirculation speed. Moreover, a thorough search of the literature

suggests that the influences of condensate on part properties in the SLM process is sparse thereby warranting an investigation to be completed.

Therefore, this study attempts to shed light regarding the influence of heat-affected powder on the tensile properties of as-built components. It was realized that heat-affected powder may not only interfere with the laser beam (condensate), but may also be redeposited onto other parts in the build area (both condensate and spatter). To observe the effect of both, the pump speed was varied and a region upstream of the tensile specimens was selectively melted for condensate production (Figure 1). In addition to the tensile properties, part porosity was measured to observe potential correlations between pore formation and degradation in strength. Since very little research characterizes heat-affected powder, samples were collected and analyzed in terms of particle size distribution and shape by using an ASPEX SEM, surface chemistry with the aid of x-ray photoelectron spectroscopy (XPS), and x-ray diffraction (XRD) for insight into crystal structure. These results were then compared to the base powder in addition to powder samples collected around the parts built in various locations.

2. EXPERIMENTAL

The starting powder used was a plasma spheroidized 304L stainless steel powder purchased from LPW. The chemical composition of the powder as provided by LPW is given in Table 1. Prior to being placed in the SLM machine, the powder was passed through a 63 μm mesh sieve that had been purged with argon gas. Once sieved, the powder was processed using a Renishaw AM250 SLM machine which contained a pulsed

Nd-YAG laser with a Gaussian profile beam intensity and a wavelength of 1070 nm. After calibrating the focal offset of the laser, the diameter of the beam spot on the powder bed was approximately 70 μm.

Table 1: Chemical composition of the base 304L stainless steel powder.

Element	C	Cr	Cu	Fe	Mn	N	Ni	O	P	S	Si
Wt %	0.015	18.5	< 0.1	69.3	1.4	0.09	9.9	0.02	0.012	0.004	0.63

Four builds were completed in order to study the effect of the heat-affected powder on the built parts. In each of the builds, a stack of Automated Ball Indenter (ABI) tensile specimens 20 mm tall were built at 5 different locations across the diagonal of the build chamber. ABI tensile specimens have a 1" (25.4 mm) total length with a 0.3" (7.6 mm) reduced gauge section and a thickness of 0.06" (1.5 mm). Build 1 incorporated a nominal pump speed (≈ 400 ft^3/min) while Build 2 had a lower pump speed (≈ 210 ft^3/min). Builds 3 and 4 incorporated extra square parts to the right of the build chamber to act as heat-affected powder generators. As before, Build 3 had a higher pump speed and Build 4 had a lower pump speed. The geometry of these builds is shown in Figure 1. After the build was completed, powder samples at each location were collected as well as samples of powder to the left of the build area, in Location F, where visibly different powder had been noticed in previous experiments. A band saw was used to remove the tensile specimen stacks from the build plate and an EDM was used to make five tensile specimens at each location (a total of 100 tensile specimens) that were approximately 1.5 mm thick.

Morphological characterization was performed using an ASPEX 1020 SEM equipped with automated feature analysis (AFA) to determine the projected area and perimeter of each particle in a given powder sample for a sample of sieved 304L SS and a sample taken from Location F. Additional characterization was performed on the sieved 304L SS sample as well as the powder samples taken from Location A - F was also performed using a Panalytical X'pert Pro Multi-Purpose Diffractometer for insight into the particle microstructure. The surface of the powder particles was studied with a Kratos Axis 165 Photoelectron Spectrometer XPS instrument where the sample was sputtered for 1 minute prior to spectral acquisition.

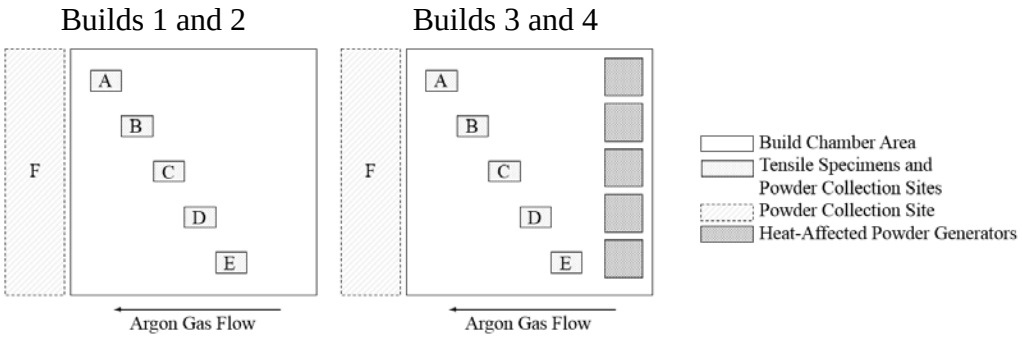

Figure 1: Experimental setup of the four builds. Builds 1 and 3 were built using nominal argon gas pump speed and Builds 2 and 4 were built using a reduced argon gas pump speed.

Characterization of the as-built parts included tensile tests which were performed using an Automated Ball Indenter (ABI) Universal Testing Machine with a constant strain rate of 4.77×10^{-4} s^{-1}. Tensile specimens were ground with 320 and 600 grit abrasive paper prior to testing. Density measurements were taken in accordance with ASTM B311 as well as surface roughness measurements using a Hirox KH-8700 Digital

Microscope. Specimens were also polished and electrolytically etched for 6 seconds using a 60:40 volume percent of nitric acid to water and 1 V. Optical micrographs were then obtained using a Nikon Epiphot 200 Microscope to compare the resulting microstructure.

3. RESULTS AND DISCUSSION

3.1. POWDER CHARACTERIZATION

Powder samples were first analyzed using the ASPEX 1020 SEM. Figure 2 shows a comparison of the base 304L SS powder and powder that was found in Location F of the build chamber. Overall, the heat-affected powder was morphologically similar in that it was still spherical. However, some anomalous particles were observed that appeared to have dark spots covering the surface. A standardless energy dispersive x-ray spectroscopy (EDS) point scan was performed on the particles with dark spots which indicated a higher amount of silicon and manganese content compared to the base powder.

The appearance of dark regions on the surface of condensate particles with the knowledge that silicon and manganese have a high affinity for oxygen suggests that these are oxide islands. A similar phenomenon was reported by Simonelli et al. [22] for 316L stainless steel in studying the formation of laser spatter. Although condensate is inherently different from laser spatter in that it forms from a metallic vapor cloud instead of solidifying from a molten state in the build chamber atmosphere, it appears that the formation of these oxide islands is related primarily to the extremely high temperatures

encountered by these particulates. Even with the small solidification times experienced, it is possible that the temperature is large enough to cause a significant amount of silicon and manganese diffusion to the outer surfaces of the particles. However, the thickness of the oxides is still unknown and will require further investigation.

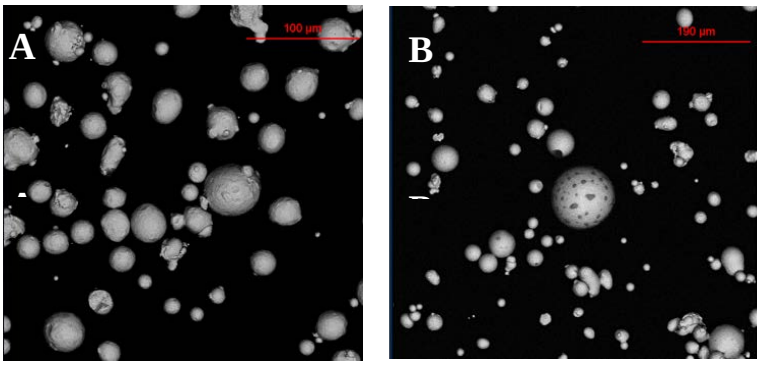

Figure 2: SEM micrographs of (A) sieved 304L stainless steel powder and (B) the heat-affected powder collected from Location F.

Particle size distributions (both number distribution and frequency distribution) obtained using the ASPEX SEM's AFA are shown in Figure 3. For each sample, over 6000 powder particles were sampled to obtain the distribution. The heat-affected powder contained particles that were larger than any found in the base 304L SS powder, where the largest particle (84 µm) was 30 µm larger than the largest particle found in the base 304L SS powder. At this point, it is important to note that the sampling of the heat-affected powder was done close to the gas flow exit. In this location it is likely that the larger heat-affected particles were only collected as they were not small enough to deposit on the surfaces of the build chamber or pass through the filter. Although this skews the measured particle size distribution, it is noteworthy that the large heat-affected

particles are most likely dispersed throughout the powder bed while the smaller particles remain in the chamber atmosphere. The presence of large particles could indicate that this heat-affected powder contains spatter, however it could also be due to agglomeration of the fine condensate particles as well. Circularity values were also found for each of the powder samples and the values for the base 304L SS powder and the powder obtained from Location F were 0.88 and 0.84, respectively.

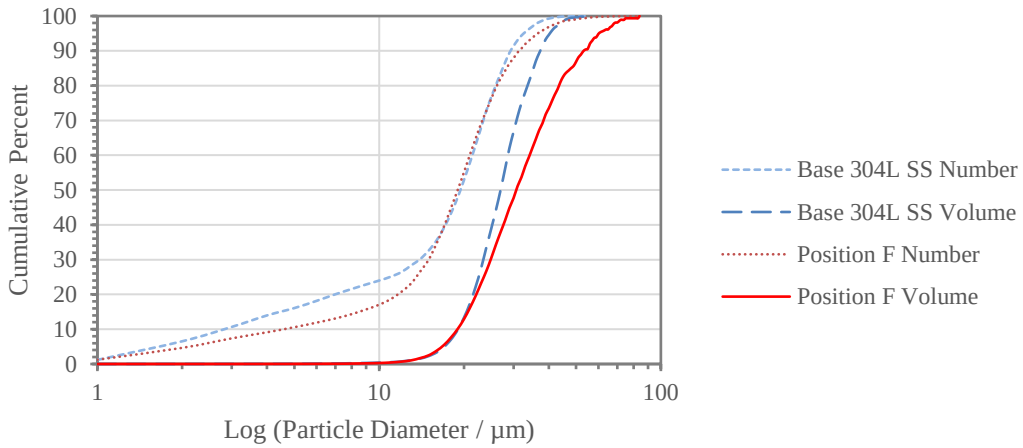

Figure 3: Cumulative number and frequency particle size distributions for the base 304L SS powder and the heat-affected powder found in Location F.

Figure 4 shows the XRD spectra of the base 304L stainless steel powder compared to the powder collected from Location F from each of the 4 builds. The XRD spectra reveals that while the base 304L SS powder is completely γ-austenite, the heat-affected powders from Location F all have varying degrees of δ-ferrite in their microstructure. This result shows that this powder has been heated to the point of melting, and upon solidification the transformation from δ-ferrite to γ-austenite was kinetically inhibited due to the high cooling rate [28]. The spectra show that there are

different amounts of the δ-ferrite in the samples, indicating varying amounts of heat-affected powder. Compared to Build 2, Build 1 had a higher argon flow rate. This enabled more of the heat-affected powder to exit the build chamber through the hole on the left wall, whereas it was simply collected in Build 2. Builds 3 and 4 follow the same logic, however the concentration of δ-ferrite in these samples is higher due to the extra parts built that generated more heat-affected powder. XRD spectra were also collected on various powder samples from Locations A-E of several builds, however only peaks corresponding to γ-austenite were found. Therefore, if there was a difference, it was not detectable by XRD.

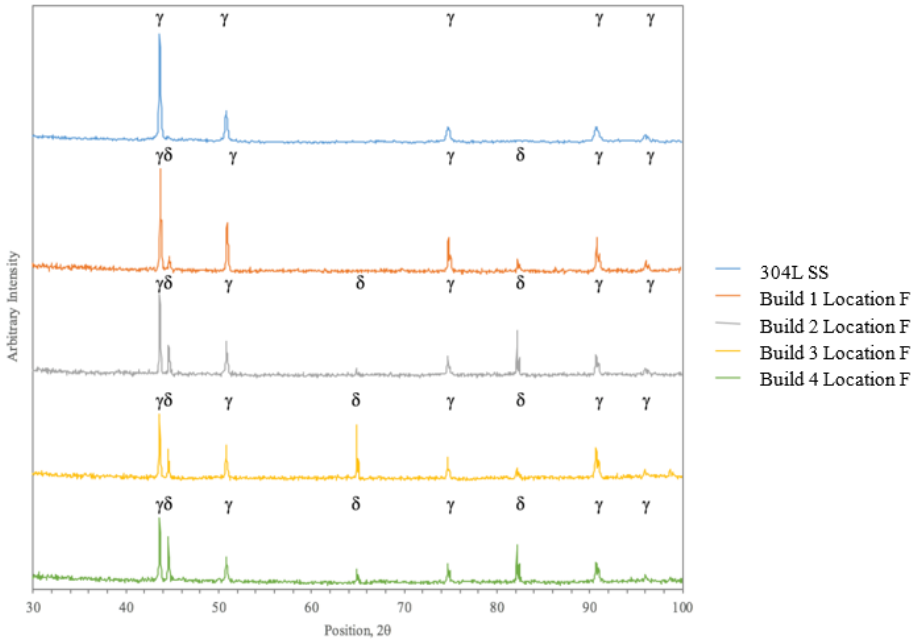

Figure 4: XRD spectra of the base 304L SS powder and the powder from Location F of each of the four builds.

XPS samples were taken from a small number of powder samples due to the time and cost of the instrument. The samples consisted of base 304L SS powder, powder from Location F, 2E, 3E, 4A, and 4E. The results from the survey spectra of the XPS analysis are summarized in Table 2. First, these results show how different the surface layers of the powder particles are to the bulk chemistry (shown in Table 1). The high content of carbon is likely due to contamination from carbon that had condensed on the sample from the air. The other concentrations indicate that the detected photoelectrons were ejected from the oxide layer. Powder samples taken from inside the build chamber showed chemistry that was more consistent with the base 304L SS powder, although decreases in Mn were observed in Build 4 Locations A and E. Slight increases in oxygen were also found in Build 3 Location E as well as Build 4 Locations A and E. When comparing the data from different locations, the main element that is changed is Si, where the concentration is increased in the heat-affected powder. The extra Si could only come from two places, namely, inside the powder particle or outside the powder particle. Although the initial concentration of Si was only 0.63 wt. %, it is possible due to the high temperatures experienced by the condensate that diffusion through the bulk occurred, as has been noted as a possibility due to the high volatility of Si [22]. The wiper in the Renishaw AM250 is made of silicone, which could provide a possible source for the extra Si. High resolution spectra were taken for Cr, Mn, Si, and Fe, although these did not reveal any significant differences between the oxidation states of the elements in the powder particles.

Table 2: Results from the survey spectra of the XPS analysis on various powder samples.

Element	304L SS	Location F	2E	3E	4A	4E
C	5	6	5	4	8	5
O	28	33	28	31	32	32
N	-	-	-	-	1	-
Ni	-	-	-	3	-	-
Si	5	19	5	6	5	5
Cr	6	6	8	10	10	13
Mn	20	17	20	17	9	11
Fe	37	18	36	37	35	33

3.2. PART CHARACTERIZATION

Samples from all locations of the four builds were polished and etched and, in order for a comparison, the optical micrographs from Location E are shown in Figure 5. The build direction is coming out of the page, so the micrographs show the hatch spacing. What can be easily seen from these micrographs is that Builds 1 and 3, with the higher argon gas flow rate, had less porosity than Builds 2 and 4, although some porosity was found in all of the specimens. Very large pores were prevalent in Location D and E of Builds 2 and 4, where the degree of porosity was worse for Build 4, where the extra parts were built to generate more condensate powder.

The results from the tensile tests are shown in Table 3. For each build and location, the values shown are the average of 5 different tensile tests. For all locations in Build 1, both yield strength and UTS values are consistent within a 95% confidence interval. However, in Builds 2 and 4, Locations D and E show a statistically significant decrease in properties. Consider Location E, where corresponding micrographs are shown in Figure 5. When looking at yield strength, for example, 2E and 4E both show a decrease compared to 1E and 3E. Comparing this to the optical micrographs and the

porosity that is present, it is obvious that the porosity had a detrimental effect on the part properties. Considering Build 4, the extra parts paired with the lower argon flow rate could lead to lowered part properties by redepositing some heat-affected powder onto other nearby parts. However, the decrease in properties for Build 2 is harder to explain. If it was just re-deposition of heat-affected powder due to the slow argon flow rate, it would be expected that this would be found in all locations, because none of the parts are down stream of other parts. It would also be expected at the left of the build chamber because large amounts of condensate powder are found just to the left of the build chamber. Theories for the location of the decrease in properties are offered at the end of this section. The results of the density measurements compared with yield strength and UTS are shown in Figure 6, where they are grouped by location in the build chamber and

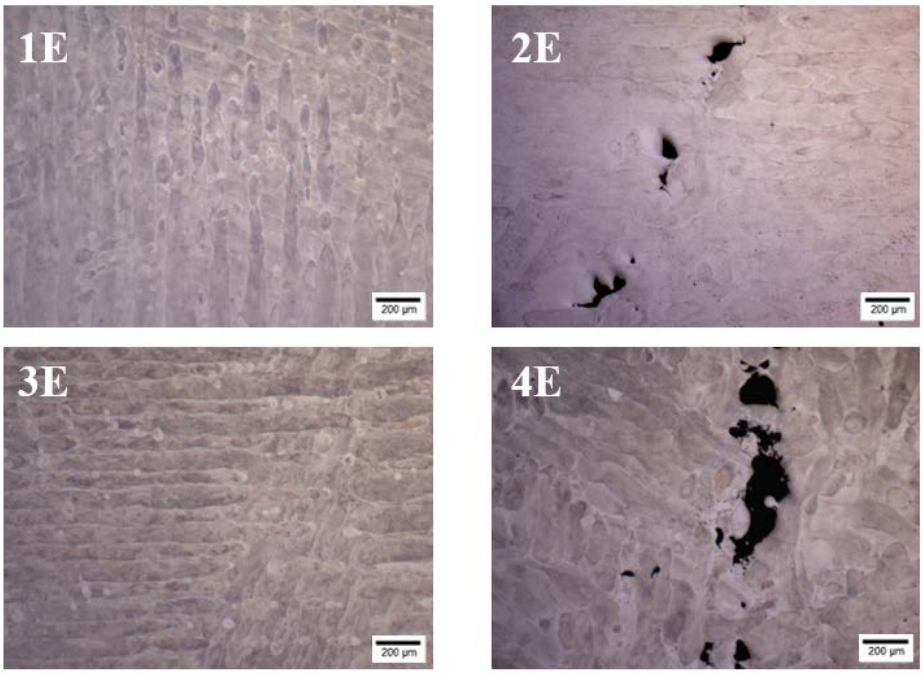

Figure 5: Optical micrographs of samples taken from Location E of each of the four builds. The print direction for these builds is coming out of the page.

patterns were used for the relative density to ease in the interpretation of the results. The relative density was calculated compared to the skeletal density of the 304L stainless steel SLM material (7.95 g/cc). The density measurements show that Location E shows the lowest densities compared to the other locations of the same build when considering Builds 2, 3, and 4, where the decrease was more drastic for Builds 3 and 4. This reveals that the location compared to other parts is an important factor. Additionally, Build 4 shows the lowest densities at every location, indicating that the gas flow rate is also a critical factor when multiple parts are being built. The density measurements correlate well with the yield strength and UTS values, where a lower density results in a decrease of strength for all cases.

Finally, surface roughness measurements were taken on the four builds at each location on surfaces perpendicular to the build direction. The results from this analysis are shown in Figure 7, where the value R_z represents the difference between the bottom and the top most surface. There is some variation across the locations of the builds; however, the obvious difference lies in Build 4, where higher surface roughness values were recorded for every location. This shows that when parts are at the same location with respect to the argon gas flow, there can be adverse effects on the final part surface finish. Build 4 Location E had the highest surface roughness values likely due to it being the closest to the extra parts that were built.

Table 3: Tensile testing results for each location of the four builds.

	Elongation (%)	Area Reduction (%)	Yield Strength (MPa)	UTS (Mpa)
1A	51.8 ± 0.99	58.4 ± 2.86	486 ± 2.72	666 ± 1.67
1B	55.3 ± 3.82	59.3 ± 3.13	484 ± 3.58	669 ± 3.83
1C	54.5 ± 3.14	58.3 ± 1.27	477 ± 1.97	662 ± 2.73
1D	53.7 ± 1.40	57.2 ± 3.05	474 ± 1.04	654 ± 4.83
1E	53.0 ± 0.97	57.5 ± 1.40	480 ± 2.98	668 ± 2.45
2A	54.4 ± 2.733	60.8 ± 2.54	477 ± 2.78	666 ± 1.78
2B	55.9 ± 2.953	59.7 ± 1.85	477 ± 4.80	659 ± 5.19
2C	54.2 ± 3.182	57.8 ± 1.28	481 ± 1.41	666 ± 2.69
2D	53.4 ± 2.64	58.6 ± 1.11	467 ± 4.24	656 ± 6.52
2E	46.8 ± 2.071	57.8 ± 2.54	447 ± 1.63	623 ± 1.90
3A	57.1 ± 1.813	60.2 ± 1.45	485 ± 4.19	664 ± 2.75
3B	55.7 ± 2.888	61.3 ± 2.26	483 ± 6.04	668 ± 5.23
3C	56.5 ± 2.056	57.7 ± 1.50	491 ± 2.52	676 ± 2.28
3D	55.1 ± 3.311	58.2 ± 0.96	472 ± 5.04	650 ± 3.69
3E	54.7 ± 0.882	58.2 ± 2.64	479 ± 4.88	654 ± 6.69
4A	53.4 ± 1.405	62.4 ± 1.79	470 ± 4.40	645 ± 5.53
4B	53.1 ± 1.867	59.7 ± 1.39	474 ± 4.09	646 ± 4.36
4C	53.3 ± 2.868	59.2 ± 0.65	464 ± 4.81	635 ± 7.38
4D	52.1 ± 2.467	53.9 ± 2.24	451 ± 3.22	629 ± 4.01
4E	41.5 ± 3.889	47.2 ± 5.18	427 ± 2.16	596 ± 6.00

Based on the results, it can be noted that the gas flow rate as well as the location of the parts relative to other parts are important aspects in the SLM process. When parts are downstream of other parts, the heat-affected powder can re-deposit on nearby locations thereby increasing local layer thicknesses [25]. This decreases the energy density thereby resulting in an increase in part porosity that is ultimately detrimental to the final part properties. However, this study yielded an unexpected result in that large amounts of heat-affected powder are collected to the left of the build chamber (Location F), so it was thought that the left side of the chamber would have more adverse effects due to the heat-affected powder. However, it was found that Locations D and E saw the

most significant decrease in properties. Therefore, there has to be some other phenomenon occurring during the process. One possibility is that there could be turbulent flow in the build chamber. The Renishaw AM 250 allows gas to flow through 6 valves, not just at one specific location. So the gas could be interacting with gas from other nozzles causing some undesirable effects. Another possibility is that during the build process, the formation of condensate powder clouds de-focus the laser in addition to beam attenuation. At different locations, the laser beam has different interactions with the condensate cloud. If this is the case, the right side of the build chamber has some aspect that induces the interaction of the condensate cloud and the laser. More studies are necessary to determine the cause of why Locations D and E were the most effected.

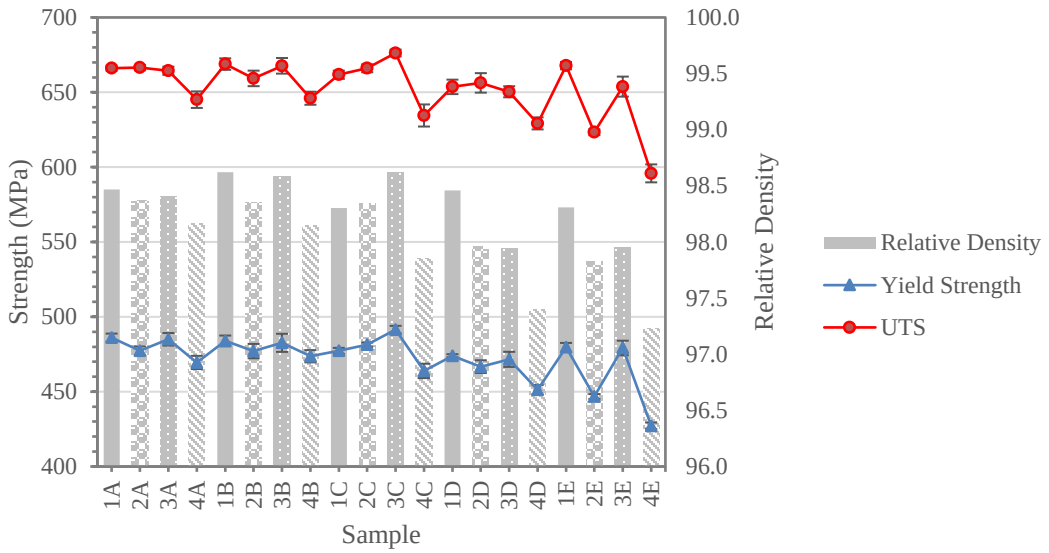

Figure 6: Comparison of the ultimate tensile strength, yield strength, and relative density.

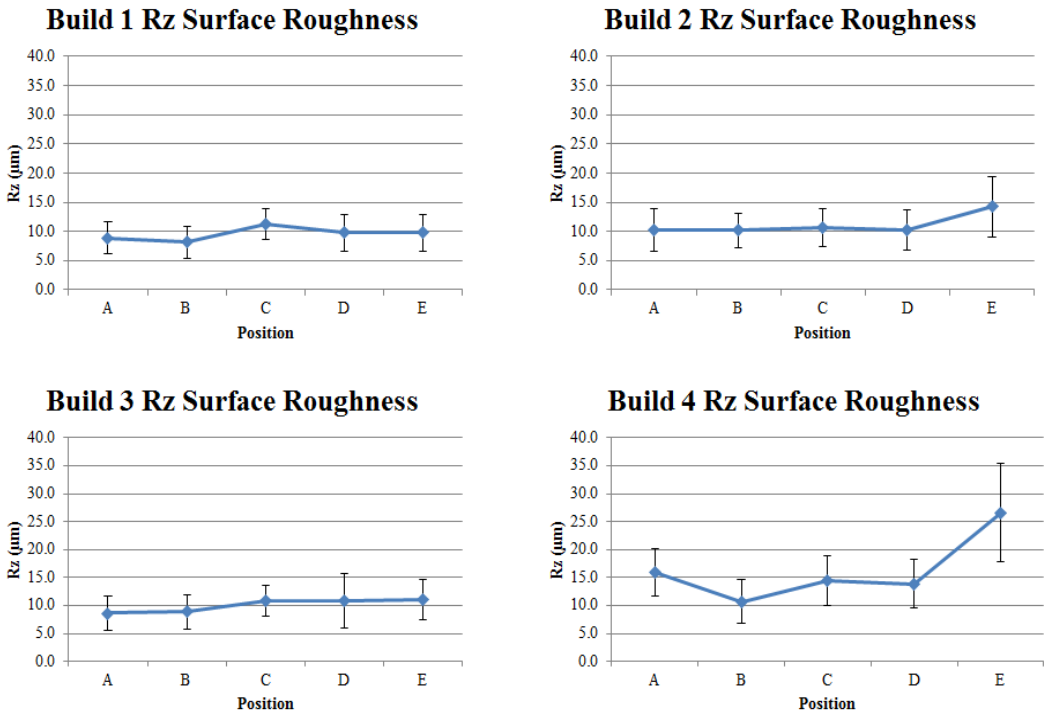

Figure 7: R_z surface roughness measurement for the four builds at each location.

4. CONCLUSIONS AND FUTURE WORK

The powder characterization study described in this paper showed that the powder collected to the left of the build chamber does contain some large particles as a consequence of particle agglomeration and possibly laser spatter. In addition to the fines being deposited on the chamber walls and being captured in the gas flow filter, this ultimately skews the particle size distribution towards being coarser than the base powder. As such, there is likely a deposition of large particles that occurs in each layer during the build process potentially shifting the average particle size of the powder with continued reuse. The average circularity values show a 5% difference between the base powder and the condensate, where there is a decrease from 0.88 to 0.84, respectively.

XRD values indicate that powder collected from the left side of the build chamber has been heated to at least the point of melting, where the fast cooling rate resulted in retained δ-ferrite in the microstructure. XRD was unable to detect any δ-ferrite on powder samples taken from Locations A-E. XPS analysis on a small amount of samples showed that the surface layers of samples taken from 2E, 3E, 4A, and 4E did not have the elevated Si content that was found in the heat-affected powder from Location F, although decreases in Mn were observed. In the future, a bulk chemistry analysis using ICPS will be performed to enable other insights to the changes that the powder underwent. A study to pinpoint how the levels of Si are so elevated in the heat-affected powder need to be conducted also.

Part characterization revealed that porosity was found in all of the built parts, where large pores could be found in builds and locations such as 2E, 4D, and 4E. Tensile tests were able to detect differences within a 95% confidence interval in Location E for Builds 2 and 4 compared to the other locations of the same build. Tensile tests also revealed that Build 1 showed consistency while Build 4 showed a decrease in UTS for all locations compared to the same locations for Builds 1-3. Density measurements were in agreement with the tensile results, where the common phenomena of lower density corresponded well to a decrease in strength. Finally, the surface roughness showed that Build 4 had a rougher surface finish on sides perpendicular to the build direction. Bulk chemistry verifications of the built parts will be completed in the future to see if the chemistry is different due to re-deposited powder.

Although the results were consistent with each other, they were not entirely expected. It was initially thought that the left side of the build chamber would see the

most re-deposited heat-affected powder as large amounts of heat-affected powder are found to the left of the build chamber, in Location F. However, Locations D and E showed a larger decrease in properties. This shows that it is not simply the gas flow controlling how the heat-affected powder is redeposited. Further studies into why Locations D and E are inferior to other locations must be performed to pinpoint the reason for this observation.

ACKNOWLEDGEMENTS

This work has been funded by Honeywell Federal Manufacturing & Technologies under Contract No. DE-NA0002839 with the U.S. Department of Energy. The United States Government retains and the publisher, by accepting the article for publication, acknowledges that the United States Government retains a nonexclusive, paid up, irrevocable, world-wide license to publish or reproduce the published form of this manuscript, or allow others to do so, for the United States Government purposes.

REFERENCES

[1] N. Guo and M. C. Leu, “Additive manufacturing: Technology, applications and research needs,” *Front. Mech. Eng.*, vol. 8, no. 3, pp. 215–243, 2013.

[2] E. C. Santos, M. Shiomi, K. Osakada, and T. Laoui, “Rapid manufacturing of metal components by laser forming,” *Int. J. Mach. Tools Manuf.*, vol. 46, no. 12–13, pp. 1459–1468, 2006.

[3] C. W. Hull, “Apparatus for production of threedimensional objects by stereolithography,” U.S. patent no. 4575330, 1986.

[4] J. P. Kruth, “Material Incress Manufacturing by Rapid Prototyping Techniques,” *CIRP Ann. - Manuf. Technol.*, vol. 40, no. 2, pp. 603–614, 1991.

[5] A. Simchi, “The role of particle size on the laser sintering of iron powder,” *Metall. Mater. Trans. B*, vol. 35, no. 5, pp. 937–948, 2004.

[6] L. Thijs, F. Verhaeghe, T. Craeghs, J. Van Humbeeck, and J. P. Kruth, “A study of the microstructural evolution during selective laser melting of Ti-6Al-4V,” *Acta Mater.*, vol. 58, no. 9, pp. 3303–3312, 2010.

[7] M. Averyanova, E. Cicala, P. Bertrand, and D. Grevey, “Experimental design approach to optimize selective laser melting of martensitic 17-4 PH powder: part I – single laser tracks and first layer,” *Rapid Prototyp. J.*, vol. 18, no. 1, pp. 28–37, 2012.

[8] L. E. Murr *et al.*, “Microstructures and properties of 17-4 PH stainless steel fabricated by selective laser melting,” *J. Mater. Res. Technol.*, vol. 1, no. 3, pp. 167–177, 2012.

[9] X. Zhao, J. Chen, X. Lin, and W. Huang, “Study on microstructure and mechanical properties of laser rapid forming Inconel 718,” *Mater. Sci. Eng. A*, vol. 478, no. 1–2, pp. 119–124, 2008.

[10] K. Abd-Elghany and D. L. Bourell, “Property evaluation of 304L stainless steel fabricated by selective laser melting,” *Rapid Prototyp. J.*, vol. 18, no. 5, pp. 420–428, 2012.

[11] E. O. Olakanmi, “Selective laser sintering/melting (SLS/SLM) of pure Al, Al-Mg, and Al-Si powders: Effect of processing conditions and powder properties,” *J. Mater. Process. Technol.*, vol. 213, no. 8, pp. 1387–1405, 2013.

[12] B. Liu, R. Wildman, C. Tuck, I. Ashcroft, and R. Hague, “Investigation the Effect of Particle Size Distribution on Processing Parameters Optimisation in Selective Laser Melting Process,” *Sff*, no. mm, pp. 227–238, 2011.

[13] M. Averyanova, P. Bertrand, and B. Verquin, “Influence of metallurgical aspects of martensitic stainless steel powder on final parts properties manufactured by Selective Laser Melting technology,” *Proceedings of the PM2010 Powder Metallurgy World Congress, 10th – 14th October 2010, Florence, Italy Published by: European Powder Metallurgy Association, 2010*. pp. 2-9, 2010.

[14] M. Averyanova, P. Bertrand, and B. Verquin, “Studying the influence of initial powder characteristics on the properties of final parts manufactured by the selective laser melting technology,” *Virtual Phys. Prototyp.*, vol. 6, no. 4, pp. 215–223, 2011.

[15] S. F. Franzen, M. Svensson, I. Elfstrom, U. Ackelid, and I. Elfstrom, “Influence of powder size and layer thickness on the properties of Ti-6Al-4V lattice structures manufactured by electron beam melting,” *European International Powder Metallurgy Congress and Exhibition, Euro PM 2011, October 9, 2011 - October 12, 2011*, vol. 2. pp. 825–834, 2011.

[16] L. C. Ardila *et al.*, “Effect of IN718 Recycled Powder Reuse on Properties of Parts Manufactured by Means of Selective Laser Melting,” *Phys. Procedia*, vol. 56, pp. 99–107, 2014.

[17] V. Seyda, N. Kaufmann, and C. Emmelmann, “Investigation of Aging Processes of Ti-6Al-4 V Powder Material in Laser Melting,” *Phys. Procedia*, vol. 39, pp. 425–431, 2012.

[18] S. A. Khairallah and A. Anderson, “Mesoscopic simulation model of selective laser melting of stainless steel powder,” *J. Mater. Process. Technol.*, vol. 214, no. 11, pp. 2627–2636, 2014.

[19] D. Dai and D. Gu, “Thermal behavior and densification mechanism during selective laser melting of copper matrix composites: Simulation and experiments,” *Mater. Des.*, vol. 55, pp. 482–491, 2014.

[20] A. V. Gusarov and I. Smurov, “Modeling the interaction of laser radiation with powder bed at selective laser melting,” *Phys. Procedia*, vol. 5, no. PART 2, pp. 381–394, 2010.

[21] F. Verhaeghe, T. Craeghs, J. Heulens, and L. Pandelaers, “A pragmatic model for selective laser melting with evaporation,” *Acta Mater.*, vol. 57, no. 20, pp. 6006–6012, 2009.

[22] M. Simonelli *et al.*, “A Study on the Laser Spatter and the Oxidation Reactions During Selective Laser Melting of 316L Stainless Steel, Al-Si10-Mg, and Ti-6Al-4V,” *Metall. Mater. Trans. A*, 2015.

[23] M. J. Zhang, G. Y. Chen, Y. Zhou, S. C. Li, and H. Deng, “Observation of spatter formation mechanisms in high-power fiber laser welding of thick plate,” *Appl. Surf. Sci.*, vol. 280, pp. 868–875, 2013.

[24] Y. Liu, Y. Yang, S. Mai, D. Wang, and C. Song, “Investigation into spatter behavior during selective laser melting of AISI 316L stainless steel powder,” *Mater. Des.*, vol. 87, pp. 797–806, 2015.

[25] A. Ladewig, G. Schlick, M. Fisser, V. Schulze, and U. Glatzel, “Influence of the shielding gas flow on the removal of process by-products in the selective laser melting process,” *Addit. Manuf.*, vol. 10, pp. 1–9, 2016.

[26] B. Ferrar, L. Mullen, E. Jones, R. Stamp, and C. J. Sutcliffe, “Gas flow effects on selective laser melting (SLM) manufacturing performance,” *J. Mater. Process. Technol.*, vol. 212, no. 2, pp. 355–364, 2012.

[27] P. Shcheglov, S. Gumenyuk, I. Gornushkin, M. Rethmeier, and V. Petrovskiy, “Vapor–plasma plume investigation during high-power fiber laser welding,” *Laser Phys.*, vol. 23, no. 1, 2013.

[28] G. R. Mirshekari, E. Tavakoli, M. Atapour, and B. Sadeghian, “Microstructure and corrosion behavior of multipass gas tungsten arc welded 304L stainless steel,” *Mater. Des.*, vol. 55, pp. 905–911, 2014.

II. EFFECT OF AREA FRACTION AND PART SPACING ON DEGRADATION OF 304L STAINLESS STEEL POWDER IN SELECTIVE LASER MELTING

Caitlin S. Kriewall[1], Austin T. Sutton[2], Sreekar Karnati[2], Joseph W. Newkirk[1], Ming C. Leu[2]

[1]Department of Materials Science and Engineering, Missouri University of Science and Technology, Rolla, MO 65409

[2]Department of Mechanical and Aerospace Engineering, Missouri University of Science and Technology, Rolla, MO 65409

(Solid Freeform Fabrication Symposium Conference Proceedings, 2017)

ABSTRACT

In selective laser melting (SLM) systems, a large portion of powder remains unconsolidated and therefore recycling powder could make SLM more economical. Currently, a lack of literature exists specifically targeted at studying the reusability of powder. Furthermore, the definition of powder reusability is complex since powder degradation depends on many factors. The goal of the current research is to investigate the effects of area fraction and part spacing on the degradation of 304L powder in SLM. An experimental study was conducted where various area fractions and part distances were chosen and powder characterization techniques for determination of particle size distributions, tap and apparent densities, and x-ray diffraction were employed to track evolving powder properties for the purpose of reuse. The results show that the recyclability of 304L powder depends on the utilization of the build area causing varying degrees of particle size coarsening and delta ferrite formation.

1. INTRODUCTION

Selective laser melting (SLM) is a powder bed fusion additive manufacturing (AM) technique where parts are built layer by layer. In this process, powder is dispensed and spread over a build plate with a predetermined thickness. A laser is then scanned over locations specified by a CAD model to consolidate the powder. After completion of the layer, the build plate is incremented down by one layer thickness and the process is repeated until the final part dimensions are achieved [1]. AM has attracted the interest of several industries due to its ability to make near net shaped parts with complicated geometry that are not attainable with subtractive processing technologies. However, powder bed processes inherently have a significant percentage of powder that is leftover after processing, as generally only 10%-50% of the build area is used for parts. Therefore, there is an opportunity to reuse this leftover powder, which would benefit the economy of the process as currently 5-46% of the cost of the SLM process is attributed to material costs [2]. However, powder characteristics and their effect on part properties must be well understood before widespread reuse of powder can be implemented.

Although sparse, there are some studies in the literature on the recyclability of certain metal powders including Ti64, Inconel 718, 17-4 stainless steel, and CoCr [3-5]. Tang *et al.* [3] studied the recyclability of Ti64 by creating a build of tensile specimens in an Arcam EBM system and collecting the powder after each build. The powder composition, size distribution, apparent and tap densities, flowability and morphology were examined after selected uses. They found that the powder could be reused up to 21 times with no undesirable effects on the mechanical properties. Ardila *et al.* [4] studied the

reusability of Inconel 718 on a Model Realizer SLM 250. Powder was collected after each iteration and the particle size distribution and composition was studied. Parts were also produced in order to evaluate the porosity, toughness, hardness and microstructure. It was found that the Inconel 718 powder could be reused up to 14 times with no significant effect on the part properties. Slotwinski *et al.* [5] studied the reusability of 17-4 stainless steel and CoCr powders in the SLM process. Although investigation of the mechanical properties was not discussed in this article, it was shown that reusing the powders corresponded with an increase of the particle size distribution. In all of these studies, the methodology behind the build design was not discussed; it was only presented as a certain build that was produced and iterated multiple times.

Heat-affected powders are created during the SLM process and can deposit in the build area [6]. The area of parts has an effect on the amount of heat-affected powders that are produced. As this powder has been shown to have a deleterious effect on part properties [6], the success of a recyclability study will depend on the parts that are present in the build. The effect of the area fraction and part spacing of built parts on the powder properties was investigated in this study. This approach aims to be a simple way to design a recyclability study, as each of the builds is relatively small and would take a minimal amount of powder and machine time. This preliminary study can be used to assess the effect of different area fractions on powder degradation. Then, a build can be designed that takes into account the desired specimens and area fractions where powder changes are known to occur. In this way there is a better chance of actually capturing changes in part properties. This study could also aid in pinpointing the area fractions where there begins to be an effect on the part properties, if such a dependence is present in the material.

2. EXPERIMENTAL METHODS

Gas-atomized 304L SS powder was purchased from LPW Technology with the chemical composition listed in Table 1. Prior to processing, the powder was passed through a 63 µm mesh sieve in order to breakup agglomerates and remove large particles that would have a negative effect on the layer thickness and uniformity. The powder was used to build parts on a Renishaw AM 250 SLM machine which contained a pulsed Nd-YAG laser with a Gaussian profile beam intensity and a wavelength of 1070 nm. The diameter of the beam spot on the powder bed was approximately 70 µm. The oxygen content in the build chamber was kept below 1000 ppm and the substrate temperature was held at 80°C. Finally, a constant volumetric argon gas flow of 400 ft^3/min was maintained across the build area during processing and was recirculated through the AM 250.

Table 1: Chemical composition of 304L SS powder used as the starting material in this study.

Element	C	Cr	Cu	Fe	Mn	N	Ni	O	P	S	Si
Wt%	0.018	18.4	< 0.1	Bal	1.4	0.06	9.8	0.02	0.012	0.005	0.6

Several builds were used in order to study the effect of area fraction and part spacing on the degradation of powder. Four of these builds consisted of 5x5 arrays of squares that were built at different area fractions, i.e. 12.5%, 25%, 50%, and 75% of the build chamber consisted of parts. This corresponded to squares with edge dimensions of 15 mm, 21 mm, 30 mm, and 36 mm for the 12.5%, 25%, 50%, and 75% builds. An

important note is that the area fraction corresponds to the area enclosed by the 4 bolt holes as corners and not the entire base plate. An additional three builds were conducted in order to evaluate the part spacing on the degradation of the powder. These builds used a 50% area fraction with different arrays of squares built, i.e. 7x7, 9x9, and 11x11 with part spacings of 8 mm, 6 mm, and 5 mm respectively. These builds are illustrated in Figure 1. Each of the seven builds was replicated three times in order to study how the powder characteristics change with recycling. For the first iteration of builds, the squares were built up to 5 mm tall meaning that the builds ranged in time from 4-24 hours. For each subsequent iteration, the height of the parts was decreased by 1.5 mm. Powder was collected and characterized after each build.

As this work is designed to be a relatively quick and easy way to determine builds for a more vigorous powder recycling study, a limited selection of particle characterization techniques were used and they were chosen based on the usefulness of the information and/or the ease of the measurement. The powder characterization included investigation of the particle size distributions, tap and apparent densities, and the phases present in the powder leftover from each build. Prior to any characterization, powder was mixed using a Turbula T2C mixer for a minimum of 15 minutes to ensure homogenization before sampling. Particle size distributions were obtained using an ASPEX 1020 scanning electron microscope (SEM) using the automated feature analysis (AFA) capabilities of the instrument. Each particle size distribution was generated from at least 2000 powder particles in order to establish an accurate distribution [7]. The particle size distributions were fit using JMP Pro software to obtain a 95% confidence interval of the distribution. Measurements of tap and apparent densities were conducted following ASTM standards

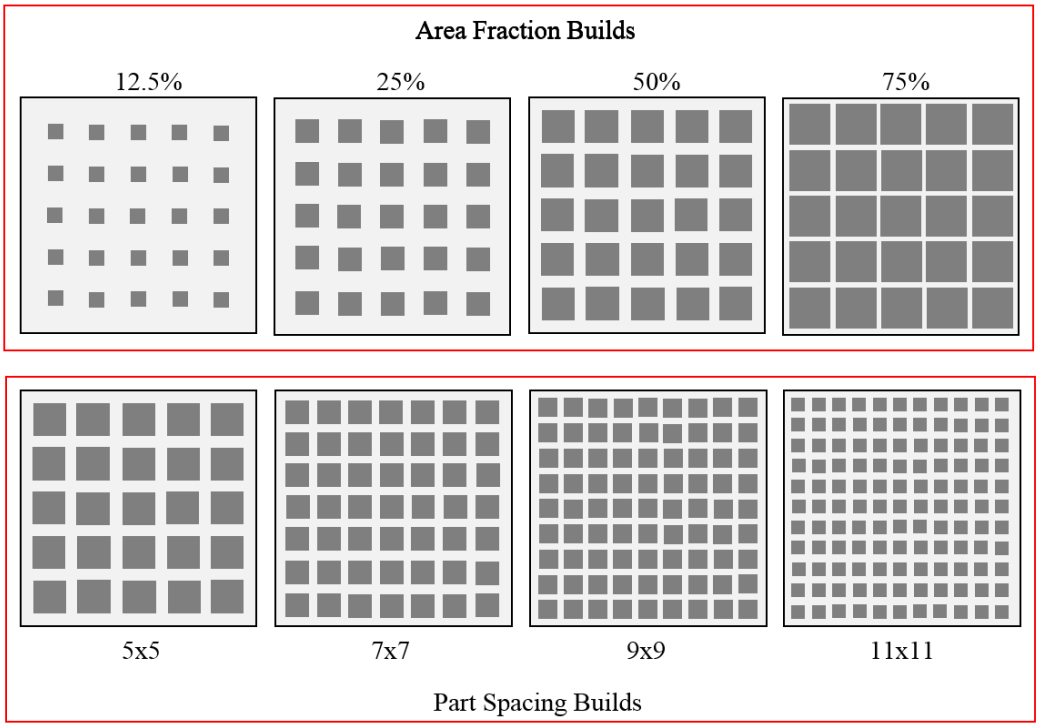

Figure 1: Illustration of the experimental builds. Note the 50% 5x5 build has been shown twice but was only completed once for each iteration. Part spacing builds were all at 50% area fraction.

B527-15 and B329-14 respectively. Each measurement of tap and apparent density was replicated three times. Determination of the percentage of phases was conducted using a Panalytical X'Pert Pro Multi-Purpose Diffractometer X-Ray Diffraction instrument. Due to the time and cost of the instrument, XRD scans were only obtained for samples of the 12.5%, 75%, 50% 5x5, and 50% 11x11 builds in order to sample the extremes. XRD scans were performed from a 2θ range of 20-100 over a 3 hour period. RIQAS 4 software was used to perform the Rietveld refinement for quantification of phases. Finally, the powder after each build was sampled for testing and sieved through a 63 µm mesh sieve before the next build and the amount of powder sieved off was documented.

3. RESULTS AND DISCUSSION

Particle size distributions have significant effects on the processing behavior of metal powders and have been shown to have an effect on the built part properties [8, 9]. The D10, D50, and D90 values from the numeric particle size distribution fit using JMP Pro are shown in Table 2. Here the plus or minus values show the 95% confidence interval. Each D-value corresponds to powder that is less than or equal to a certain size at the specified percentage. For example, the first iteration of the 12.5% area fraction build has a D50 value of 22.3 μm. This means that in the cumulative number plot, 50% of the powder was less than or equal to 22.3 μm. In order to make conclusions about the particle size distributions, the three D values must be considered together.

When considering the area fraction builds, both the D50 and D90 (shown in Figure 2 and Figure 3 respectively) values showed a statistically significant increase of the particle size between iteration 1 and 2. This increase was not observed for the D10 values, where for most cases (excluding the 50% 5x5), the D10 either was not statistically significantly different or there was a decrease observed. This coupled with the increase in D50 and D90 for the area fraction builds indicated that the particle size distributions were spreading out between iteration 1 and 2. However, this behavior was not carried into iteration 3, where the only area fraction build with a statistically significant increase in particle size distribution was the 25% build. The remaining area fraction builds showed a decrease in D90 values and either a decrease or no change in the D50 values. A trend was unable to be established for the D10 values between iteration 2 and 3. The coarsening observed between iteration 1 and 2 in the area fraction samples was not observed reliably in the part spacing

samples. The 50% 5x5 build and the associated trends were discussed with regards to the area fraction. Considering the 7x7, 9x9, and 11x11 builds, there was no trend found in the particle size distributions.

Table 2: D10, D50 and D90 values for each build and iteration.

Area Fraction	Array	D10 (µm) Iteration 1	Iteration 2	Iteration 3
12.50%	5x5	13.8 ± 0.4	12.6 ± 0.7	15.4 ± 0.6
25%	5x5	11.6 ± 0.5	12.2 ± 0.4	13.6 ± 0.6
50%	5x5	14.7 ± 0.4	23.5 ± 0.3	14.5 ± 0.5
50%	7x7	17.5 ± 0.4	13.7 ± 0.5	14.5 ± 0.6
50%	9x9	14.3 ± 0.5	14.8 ± 0.4	11.2 ± 0.8
50%	11x11	15.1 ± 0.5	13.1 ± 0.7	14.5 ± 0.5
75%	5x5	14.3 ± 0.7	13.3 ± 0.9	15.1 ± 0.6
Area Fraction	Array	D50 (µm) Iteration 1	Iteration 2	Iteration 3
12.50%	5x5	22.3 ± 0.3	24.9 ± 0.5	25.4 ± 0.4
25%	5x5	21.9 ± 0.4	23.8 ± 0.3	25.0 ± 0.5
50%	5x5	23.5 ± 0.3	28.6 ± 0.4	24.3 ± 0.4
50%	7x7	26.1 ± 0.3	25.2 ± 0.3	25.3 ± 0.4
50%	9x9	23.1 ± 0.4	24.9 ± 0.3	24.7 ± 0.6
50%	11x11	25.9 ± 0.4	24.8 ± 0.5	24.9 ± 0.4
75%	5x5	25.5 ± 0.5	28.3 ± 0.7	26.3 ± 0.5
Area Fraction	Array	D90 (µm) Iteration 1	Iteration 2	Iteration 3
12.50%	5x5	30.8 ± 0.4	37.2 ± 0.7	35.4 ± 0.6
25%	5x5	32.3 ± 0.5	35.3 ± 0.4	36.4 ± 0.6
50%	5x5	32.4 ± 0.4	39.5 ± 0.5	34.2 ± 0.5
50%	7x7	34.7 ± 0.4	36.6 ± 0.5	36.1 ± 0.6
50%	9x9	31.8 ± 0.5	34.9 ± 0.4	38.2 ± 0.8
50%	11x11	36.6 ± 0.5	36.6 ± 0.7	35.4 ± 0.5
75%	5x5	36.6 ± 0.7	43.3 ± 0.9	37.5 ± 0.6

Table 3 shows the apparent density, tap density, and Hausner ratio of powder samples for each iteration, where the apparent and tap densities are graphically displayed

in Figure 4 and Figure 5. Both the tap and apparent densities increased between iteration 1 and iteration 2 for all of the builds. Tap densities also increased between iteration 2 and iteration 3 in all cases except the 50% 9x9 build. However, the apparent densities dropped after iteration 2. With the increase of both the tap and apparent densities at iteration 2, a decrease in the Hausner ratio for certain builds (50% and 75%) was observed. The Hausner ratio is the ratio of the tap to apparent densities and serves as a simple way to describe the flowability of powders [10]. Although this ratio has been noted to be unsatisfactory in completely describing the flowability in AM processes, the decrease in Hausner ratio corresponds with improving powder flowability. Improvement of powder flowability with reuse has also been noted by other researchers using different materials [3]. This improved flowability could imply that the ideal powder may not be the virgin powder. As both the tap and apparent density values were increasing, the density of each powder layer and therefore the bed density was expected to improve as well [9]. This improved bed density could have a positive influence on the part density, as a more dense powder bed will increase the density of the part by decreasing the lack-of-fusion pores. Future work will incorporate part density measurements by Archimedes method in order to assess how the powder spreadability is changing with powder reuse.

The results of the Rietveld refinement XRD pattern fitting on the 12.5%, 75%, 50% 5x5, and 50% 11x11 builds are shown in Table 4. In this table, the weight percentage of δ-ferrite is shown as each sample only had two identifiable phases, δ-ferrite and γ-austenite. 304L SS is an austenitic stainless steel that, according to the chrome nickel equivalent, follows a ferritic-austenitic solidification path where:

$$L \rightarrow L + \delta \rightarrow L + \gamma + \delta \rightarrow \gamma + \delta \rightarrow \gamma$$

where δ is δ-ferrite and γ is γ-austenite [11]. Fast cooling is necessary to retain δ-ferrite [12] however at extremely high cooling rates (on the order of $10^5 – 10^6$), the supercooled liquid can be present below the metastable solidus and solidification by primary austenite

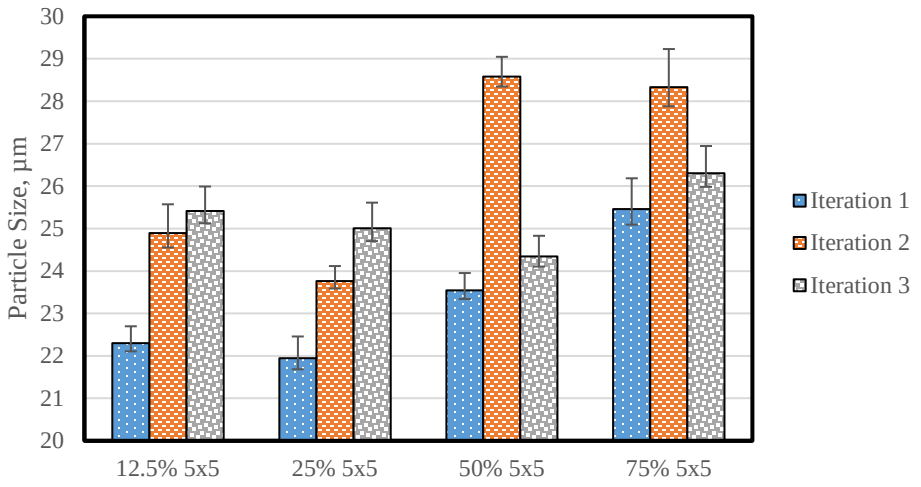

Figure 2: D50 values obtained from numeric particle size distributions for each iteration for the area fraction builds. Error bars show the 95% confidence intervals.

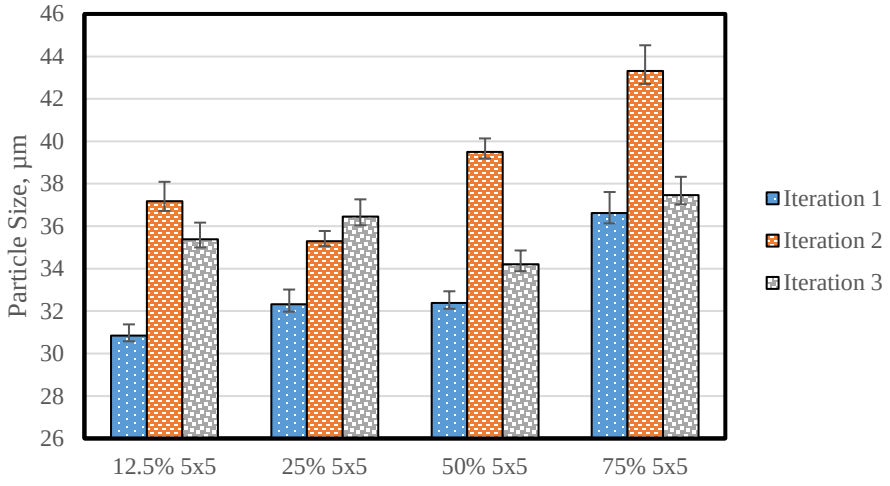

Figure 3: D90 values obtained from numeric particle size distributions for each iteration for the area fraction builds. Error bars show the 95% confidence intervals.

is possible [13]. Therefore, in the 304L SS powder processed through SLM, δ-ferrite becomes a marker of heat-affected powder, as the virgin powder has very little δ-ferrite due to the extremely high cooling rates achieved through the gas atomization process. In

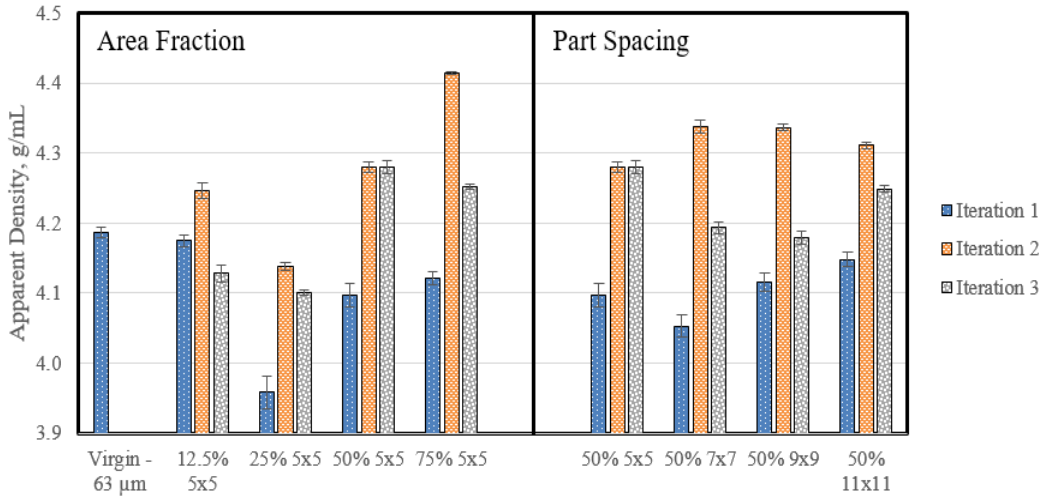

Figure 4: Apparent densities for various builds after each iteration. Error bars show the standard deviations of the three iterations.

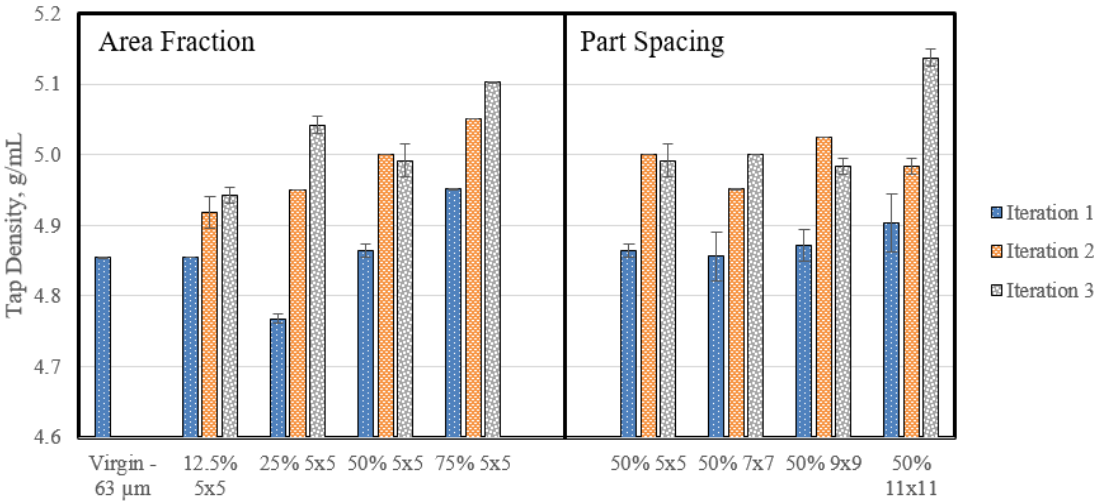

Figure 5: Tap densities for various builds after each iteration. Error bars show the standard deviations of the three iterations.

Table 3: Apparent density, tap density and Hausner ratio for each iteration of the seven builds.

Area Fraction	Array	Apparent Density		
		Iteration 1	Iteration 2	Iteration 3
12.50%	5x5	4.17 ± 0.01	4.25 ± 0.01	4.13 ± 0.01
25%	5x5	3.96 ± 0.02	4.14 ± 0.01	4.10 ± 0.00
50%	5x5	4.10 ± 0.02	4.28 ± 0.01	4.28 ± 0.01
50%	7x7	4.05 ± 0.02	4.34 ± 0.01	4.19 ± 0.01
50%	9x9	4.12 ± 0.01	4.34 ± 0.01	4.18 ± 0.01
50%	11x11	4.15 ± 0.01	4.34 ± 0.00	4.25 ± 0.00
75%	5x5	4.12 ± 0.01	4.41 ± 0.00	4.25 ± 0.00
Area Fraction	Array	Tap Density		
		Iteration 1	Iteration 2	Iteration 3
12.50%	5x5	4.77 ± 0.01	4.92 ± 0.02	4.94 ± 0.01
25%	5x5	4.86 ± 0.01	4.95 ± 0.00	5.04 ± 0.01
50%	5x5	4.86 ± 0.03	5.00 ± 0.00	4.99 ± 0.02
50%	7x7	4.87 ± 0.02	4.95 ± 0.00	5.00 ± 0.00
50%	9x9	4.90 ± 0.04	5.03 ± 0.00	4.98 ± 0.01
50%	11x11	4.95 ± 0.00	4.98 ± 0.01	5.14 ± 0.01
75%	5x5	4.85 ± 0.00	5.05 ± 0.00	5.10 ± 0.00
Area Fraction	Array	Hausner Ratio		
		Iteration 1	Iteration 2	Iteration 3
12.50%	5x5	1.16 ± 0.00	1.16 ± 0.01	1.20 ± 0.00
25%	5x5	1.20 ± 0.01	1.20 ± 0.00	1.23 ± 0.00
50%	5x5	1.19 ± 0.01	1.17 ± 0.00	1.17 ± 0.01
50%	7x7	1.20 ± 0.01	1.14 ± 0.00	1.19 ± 0.00
50%	9x9	1.18 ± 0.00	1.16 ± 0.00	1.19 ± 0.01
50%	11x11	1.18 ± 0.01	1.16 ± 0.00	1.21 ± 0.00
75%	5x5	1.20 ± 0.00	1.14 ± 0.00	1.20 ± 0.00

contrast, various kinds of heat-affected powder are present in the process due to the various interactions with the laser that have cooling rates sufficient to retain δ-ferrite [6]. For comparative purposes, the amount of δ-ferrite in the virgin 304L SS powder that had been passed through the 63 µm sieve was 1.5%.

When considering the area fraction builds (12.5% and 75%), there was an obvious difference in the amount of δ-ferrite present in the powder samples. In each iteration, the amount of δ-ferrite in the 75% build was always higher than in the 12.5% build. Both builds showed an increase, however the 75% build experienced a greater increase in δ-ferrite after each iteration. The part spacing builds are again more difficult to interpret, as there seems to be an anomalous result in the 50% 5x5 iteration 1. Comparisons between 50% 5x5 and the 11x11 builds do show that the 11x11 build has more δ-ferrite. Additionally, the amount of δ-ferrite increases with each iteration (for the 11x11 builds) and appears to increase at a faster rate than the 5x5 builds. These results showed that both the area fraction and the part spacing have an effect on the amount of heat-affected powder that is generated and deposited inside the build chamber during processing.

Table 4: Rietveld refinement results showing percentage of delta-ferrite.

Area Fraction	Array Size	Iteration 1	Iteration 2	Iteration 3
12.5%	5x5	0%	0.1%	1.3%
50%	5x5	2.2%	0.9%	1.1%
50%	11x11	4.2%	4.9%	6.1%
75%	5x5	3.6%	7.2%	11.4%

Figure 6 shows the results of the percentage of powder that was sieved off prior to being run for the next iteration. Between iteration 1 and 2, more powder was generally sieved off, although the amount sieved off for the 12.5% build stayed consistent. Furthermore, between iteration 2 and 3 the majority of the samples either stayed the same or decreased in the amount of powder sieved off, although the 50% 5x5 and 9x9 builds

still increased. This result was consistent with what was observed from the particle size distributions. When considering the different area fractions, there was a clear trend that increasing the area fraction corresponds to an increase in the amount of powder that was sieved out. Again, it was more difficult to establish a trend concerning the part spacing builds.

Powder from any of these builds has been shown to change in at least one of the characterization methods performed. However, the degree to which it changes was different for each build. For the 12.5% area fraction builds, the change was noted in the particle size distributions and tap and apparent densities, yet the XRD and percent of powder sieved off show fairly consistent powder with minor differences. On the other hand, the 75% powder showed differences in every test, however a 75% area fraction build would be difficult to justify for a recycling study as the first build would have to be repeated several times in order to generate enough powder to carry through the study. A 304L SS powder reusability study incorporating more mechanical testing and powder characterization parts will be employed. Area fractions between 25% and 50% will be used for this study, because powder in this range has detectable differences that have been shown by other researchers to have an effect on the part properties.

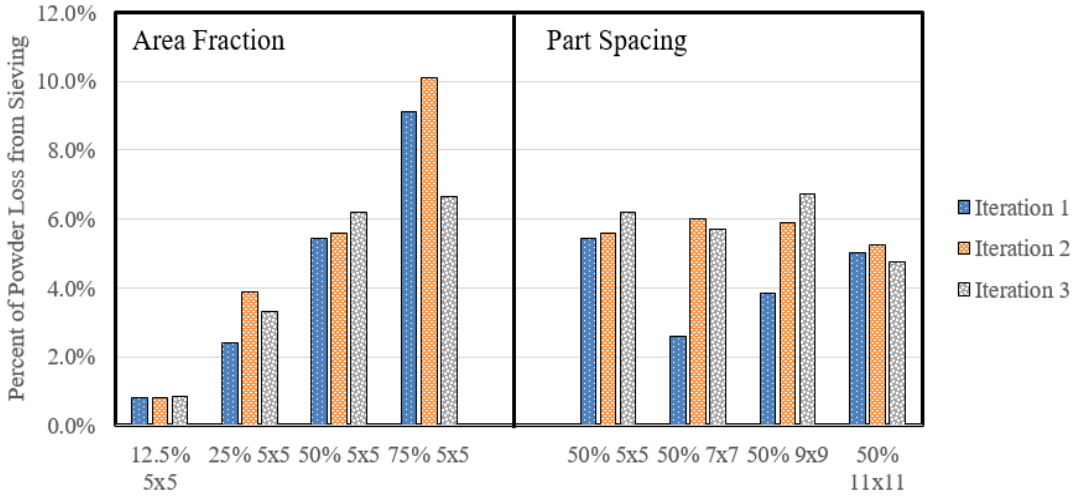

Figure 6: Percentage of powder sieved off after each iteration of builds.

4. SUMMARY OF RESULTS

Powder characterization of the area fraction builds (12.5%, 25%, 50%, and 75%) and part spacing builds (50% 5x5, 7x7, 9x9, and 11x11) that were replicated three times enabled insights into the effect of area fraction on the powder. These included that increasing the area fraction induced an increase in the D50 and D90 of the particle size distributions between iteration 1 and 2. The corresponding D10 values stayed consistent or lowered, meaning that the particle size distributions were not only coarsening, but also widening. However, this behavior was not carried into iteration 3, where particle size distributions were shown to drop, yet the D50 and D90 were still higher for iteration 3 compared to iteration 1. Tap and apparent densities both increased between iteration 1 and 2 for all of the area fraction builds. This improvement in tap and apparent densities coupled with the spreading of the powder could have an advantageous effect as the powder bed density was expected to increase. While the tap density increased further on

iteration 3, the apparent density either remained consistent or fell to a lower value for this iteration. The XRD analysis showed that the 75% area fraction had more δ-ferrite, an indication of the amount of heat-affected powder, than both the 12.5% and 50% area fraction builds. Finally, the amount of powder sieved off increased with increasing area fraction for all iterations. When comparing the same build through different iterations, the amount of powder sieved off was shown to increase between iteration 1 and 2 apart from the 12.5% area fraction that stayed consistent. Furthermore, between iteration 2 and 3 the powder sieved off was not as consistent, where 12.5% build stayed consistent, 25% and 75% decreased, and 50% increased. The amount of powder sieved was shown to change significantly for the 75% build with each iteration however the 12.5% build stayed consistent through each iteration.

Across all the powder characterization techniques employed it was more difficult to establish trends with the part spacing builds. Trends were not identifiable in the particle size distribution data. The same trends observed in the area fraction builds concerning the tap and apparent densities were observed in the part spacing builds. The XRD showed that the 11x11 builds had more δ-ferrite compared to the 5x5 build and the amount of δ-ferrite in the 11x11 build increased with each iteration. Finally, the sieving results showed no trend when comparing the different part spacing builds, however, when comparing iteration 1 to 2 there was an increase in the powder sieved off for each part spacing build. The 5x5 and 9x9 showed an increase between iteration 2 and 3 while builds 7x7 and 11x11 had a decrease.

Powder from each of the builds was shown to have differences in at least one of the characterizations performed, however the degree to which the powder changed was

different. The 75% build showed the most drastic differences, however this area fraction would be unrealistic for a more involved reusability study. For the more involved 304L SS powder reusability study, area fractions between 25% and 50% will be used given that the powders in this range did show detectable differences that could have an effect on part properties. Future work will involve powder characterization on samples post-sieving to correlate the heat-affected powder to the sieve loss. Additionally, mechanical testing will be needed to evaluate if the differences observed in the powder equate to differences in part performance. For this testing, mini-tensile specimens will be extracted at 5 locations corresponding to the diagonal across the build plate. Comparisons between each build and iteration and the different builds will be completed. Ideally, this work will provide a way to optimize the powder loss to machine productivity trade-off. Finally, a more involved 304L SS powder reusability study will be performed.

ACKNOWLEDGEMENTS

This work was funded by Honeywell Federal Manufacturing & Technologies under Contract No. DE-NA0002839 with the U.S. Department of Energy. The United States Government retains and the publisher, by accepting the article for publication, acknowledges that the United States Government retains a nonexclusive, paid up, irrevocable, world-wide license to publish or reproduce the published form of this manuscript, or allow others to do so, for the United States Government purposes. Furthermore, the authors would like to acknowledge Jeff Hill, Jacob Ficht, and Eric Bohannan for their assistance in this research.

REFERENCES

[1] A. T. Sutton, C. S. Kriewall, M. C. Leu, and J. W. Newkirk, "Powder characterisation techniques and effects of powder characteristics on part properties in powder-bed fusion processes," *Virtual Phys. Prototyp.*, vol. 12, no. 1, pp. 3–29, 2016.

[2] M. Barclift, S. Joshi, T. Simpson, and C. Dickman, "Cost modeling and depreciation for reused powder feedstock in powder bed fusion additive manufacturing," *Solid Free. Fabr. Symp.*, pp. 2007–2028, 2016.

[3] H. P. Tang, M. Qian, N. Liu, X. Z. Zhang, G. Y. Yang, and J. Wang, "Effect of Powder Reuse Times on Additive Manufacturing of Ti-6Al-4V by Selective Electron Beam Melting," *Jom*, vol. 67, no. 3, pp. 555–563, 2015.

[4] L. C. Ardila, F. Garciandia, J. B. González-Díaz, P. Álvarez, a. Echeverria, M. M. Petite, R. Deffley, and J. Ochoa, "Effect of IN718 Recycled Powder Reuse on Properties of Parts Manufactured by Means of Selective Laser Melting," *Phys. Procedia*, vol. 56, pp. 99–107, 2014.

[5] J. A. Slotwinski, E. J. Garboczi, P. E. Stutzman, C. F. Ferraris, S. S. Watson, and M. A. Peltz, "Characterization of metal powders used for additive manufacturing," *J. Res. Natl. Inst. Stand. Technol.*, vol. 119, pp. 460–493, 2014.

[6] A. Ladewig, G. Schlick, M. Fisser, V. Schulze, and U. Glatzel, "Influence of the shielding gas flow on the removal of process by-products in the selective laser melting process," *Addit. Manuf.*, vol. 10, pp. 1–9, 2016.

[7] E. Vigneau, C. Loisel, M. F. Devaux, and P. Cantoni, "Number of particles for the determination of size distribution from microscopic images," *Powder Technol.*, vol. 107, no. 3, pp. 243–250, 2000.

[8] P. K. Samal and J. W. Newkirk, "Powder Metallurgy, Metal Powder Characterization, Bulk Properties of Powders," *ASM Handb.*, vol. 7, pp. 93–168, 2015.

[9] A. B. Spierings, N. Herres, G. Levy, and C. Buchs, "Influence of the particle size distribution on surface quality and mechanical properties in AM steel parts," *Rapid Prototyp. J.*, vol. 17, no. 3, pp. 195–202, 2011.

[10] H. H. Hausner, "Friction Conditions in a Mass of Metal Powder.pdf." International Journal of Powder Metallurgy, pp. 7–13, 1967.

[11] A. F. Padilha, C. F. Tavares, and M. A. Martorano, “Delta Ferrite Formation in Austenitic Stainless Steel Castings,” *Mater. Sci. Forum*, vol. 730–732, no. Table 1, pp. 733–738, 2012.

[12] K. Guan, Z. Wang, M. Gao, X. Li, and X. Zeng, “Effects of processing parameters on tensile properties of selective laser melted 304 stainless steel,” *Mater. Des.*, vol. 50, pp. 581–586, 2013.

[13] R. N. Wright, J. E. Flinn, G. E. Korth, J. C. Bae, and T. F. Kelly, “The microstructure and phase relationships in rapidly solidified type 304 stainless steel powders,” *Metall. Trans. A*, vol. 19, no. October, pp. 2399–2405, 1988.

III. PLASMA SPHEROIDIZATION OF VITRELOY 106A BULK METALLIC GLASS POWDER

Caitlin S. Kriewall and Joseph W. Newkirk

Department of Materials Science and Engineering, Missouri University of Science and Technology, Rolla, MO 65409

(This manuscript is in preparation for submission to the *Journal of Materials Processing Technology*)

ABSTRACT

Inert ground Vitreloy 106A powder was used as the starting material for inductively coupled plasma spheroidization. The processed powders were characterized to determine their morphology, flowability, chemistry and thermal transitions. Processed powder samples were shown to have a particle size distribution that was consistent with the starting material indicating no significant agglomeration of particles occurred. The average circularity of the processed powder was increased when compared to the starting powder. This resulted in increases in both apparent and tap densities and the flowability was also shown to increase. Fine particles that were high in oxygen and copper were vaporized resulting in tightening of the chemistry distribution. XRD and DSC indicated that the starting powder was fully crystallized while the processed powder had amorphous and crystalline structures present. Raman spectroscopy was used to detect NiO on the surface of the processed powder particles. Testing indicated that the processed powder had better properties compared to the starting powder when considering flowability, amorphous content and sphericity.

1. INTRODUCTION

Bulk metallic glasses (BMGs) are multicomponent metal alloys that are devoid of crystalline microstructure. These glassy alloys are considered ‘bulk’ once fully amorphous microstructure is present in a 1 mm diameter [1]. BMGs are of interest due to their higher strengths compared to their crystalline counter parts, excellent wear and corrosion resistance due to their lack of gran boundaries and dislocations, and high fracture toughness [2]. The unique properties of metallic glasses has attracted interest, however the need for very high cooling rates limited the exploration of these alloys for many years. Through alloying additions, regions of deep eutectics can be found in multicomponent systems where crystal nucleation can be bypassed and the critical cooling rate can be reduced. One such alloy is Vitreloy 106A, a Zr-based metallic glass where the critical cooling rate is ~ 1.75 K/s [3].

Additive manufacturing (AM) techniques typically use laser or electron beam based consolidation of successive layers of powder in order to build a part in a layer-by-layer approach [4]. AM in general has attracted substantial interest in recent years due to the ability to create near net shaped parts that require little machining and allow design flexibility that is not possible with traditional manufacturing methods. AM has shown promise for manufacturing metallic glass parts due to the inherently high cooling rates associated with the process and the ability to make near net shaped parts. Several researchers have indicated that they can exceed the critical casting thickness using AM methods [5] – [7]. Another technique that uses powder feedstock is cold spray (CS) which is used to make coatings. In this process, powder and heated inert gas are pushed

through a nozzle directed at a substrate. The high kinetic energy results in the particles getting embedded into the substrate on impact [8]. CS technologies can have cooling rates on the order of 10^5-10^6 K/s and therefore researchers have recently starting using metallic glass powders for this process [9]. Both AM and CS use spherical powders, usually in the form of gas-atomized powder [9]–[13]. For exotic materials, gas-atomized powder can be extremely difficult to find and expensive. Currently there are only a few places in the United States where amorphous, gas-atomized powder can be purchased. There is a need for other methods to attain spherical powder usable in these processes.

Plasma processing shows promise for the spheroidization of metallic glass powder because of the several advantages the technology offers. Powder processed through plasma systems have increases in flowability, density and sphericity [14]. The ease of use of commercial plasma systems enable widespread use in academia and industry. Many powders have been spheroidized using plasma systems including titanium carbide [15], 316L stainless steel [16], titanium [17], tungsten and molybdenum [18]. In this study, Vitreloy 106A ($Zr_{58.5}Cu_{15.6}Ni_{12.8}Al_{10.3}Nb_{2.8}$) inert ground powder was used as the starting material to determine optimum process parameters to yield spherical metallic glass powder. This powder would then be ideal for use in a powder based AM processes, or other applications such as metal injection molding.

2. EXPERIMENTAL METHODS

Vitreloy 106A ($Zr_{58.5}Cu_{15.6}Ni_{12.8}Al_{10.3}Ni_{2.8}$) was cast by Materion. This material was then inert ground by Eutectix to produce powder in the size range of 1-135µm. Prior

to processing the powder through plasma, the powder was sieved through an 88µm sieve using a Russell sieve shaker. The powder was then mixed thoroughly using a Turbula mixer for 30 minutes. A TekSphero-15 plasma spheroidizer equipped with an inductively coupled plasma made by Tekna was used for the spheroidization of the powder. The plasma parameters are listed in Table 1. The TekSphero-15 was equipped with three chambers where powder was deposited: the reactor chamber, the cyclone, and the filter. Powder from both the reaction chamber and cyclone was collected after processing while nanopowder from the filter was discarded. It is important to note that due to the low melting point of Vitreloy 106A (~866°C [19]), a relatively low plasma power was used for processing of the powder in an attempt to reduce the amount of vaporization and agglomeration. In order to reduce the risk of combustion of nanopowder, passivation of all the powder was conducted. During processing, it was common for vaporized material to condense on the surface of solidified powder particles and coat the particles in nanopowder. Therefore, all collected powder was cleaned to remove this nanopowder. During the cleaning procedure, 10 grams of powder was placed in a beaker with 20 mL of ethanol. This beaker was then placed in an ultrasonic cleaner for 15 minutes. The larger powder particles then settled for 5 minutes and the ethanol that contained fine powder particles was decanted off. This procedure was repeated until the ethanol was clear when decanting. The powder was once again mixed using a Turbula mixer to ensure representative sampling. SEM, EDS, and Raman spectroscopy powder samples were sprinkled onto a carbon dot on a sample stub. Cross-sectioned powder samples were mounted in Polyfast conductive bakelite and polished.

Table 1: TekSphero-15 plasma parameters used for the spheroidization of inert ground Vitreloy 106A powder.

Power	Shield Gas (Ar)	Central Gas (Ar)	Secondary Gas (H_2)	Frequency	Stroke	Carrier Gas (Ar)
12 kW	40 lpm	10 lpm	2 lpm	107.0	45.0	4 lpm

Characterization of the powder included micrographs, particle size distributions, circularity measurements, flowability measurements, chemistry determinations, surface oxide characterization, identification of phases and identification of glass transition and crystallization events. An ASPEX scanning electron microscope (SEM) was used to acquire micrographs and the automated feature analysis on this microscope was used to attain the particle size and circularity information. The energy dispersive spectroscopy (EDS) on the ASPEX SEM was used for chemistry determinations. Apparent and tap densities were determined by following ASTM standards B212 and B527 respectively [20], [21]. These values were used to compute the Hausner ratio [22]. A Revolution Flowability Analyzer was used to determine avalanche angles of the powders. A PANalytical X'Pert Pro Multi-Purpose Diffractometer x-ray diffraction (XRD) instrument was used to determine degree of crystallization and identify phases in the powder. The XRD scan was performed from a 2θ range of 5–90° over a 1 hour period. A TA Instruments SDT Q600 differential scanning calorimeter (DSC) was used to determine the glass transition and crystallization events. A heating rate of 10°C/min was used up to 650°C with a constant argon gas flow rate of 100 mL/min. A HORIBA Jobin Yvon LabRAM ARAMIS Raman spectrometer was used to characterize surface oxides on spheroidized powder. The spectra were collected from a wavenumber range of 150-

1200 cm^{-1}, the hole was 500µm, the slit was 300µm, a 1200 grating was used and the collection time was approximately 5 minutes.

3. RESULTS AND DISCUSSION

Many aspects were considered when assessing the success of process parameters for spheroidization of the Vitreloy 106A powder. While the most desirable feature was the spheroidization of the powder, other factors such as the amount of material lost to processing, the particle size distribution and whether the powder was amorphous were of importance as well. During processing, 16 wt% of the powder was vaporized and was either collected in the nanochamber of the Tekna or was stuck to the walls of the main chamber. Attempts to reduce the amount of powder lost during processing resulted in the undesirable production of agglomerated particles. During cleaning, 1.5 wt% of the powder was removed.

SEM micrographs, shown in Figure 1, were acquired for the starting and plasma processed powder in order to evaluate powder morphology. It is evident from these micrographs that the starting powder had an angular morphology consistent with a ground powder with low plasticity. There was also a relatively large amount of fines present in this powder sample. In contrast, the powder after processing was visibly more spherical and a large amount of fines were removed. The reduction of fines in the processed powder can be attributed to two things. Firstly, during processing the fines were vaporized while in the high-temperature plasma and either condensed on solidified powder particles or in the nanochamber. The other reason for fine reduction is the ethanol

and ultrasonic cleaning procedure that was used on all processed powder samples. The particle size distribution information is quantitatively represented in Table 2. Here the numeric and volumetric D10, D50, and D90 values are shown. All of the numeric D-values for the processed powder are higher than the starting powder which quantitatively indicate the reduction of fines. The volumetric D90 values have similar values which indicate that significant agglomeration did not take place.

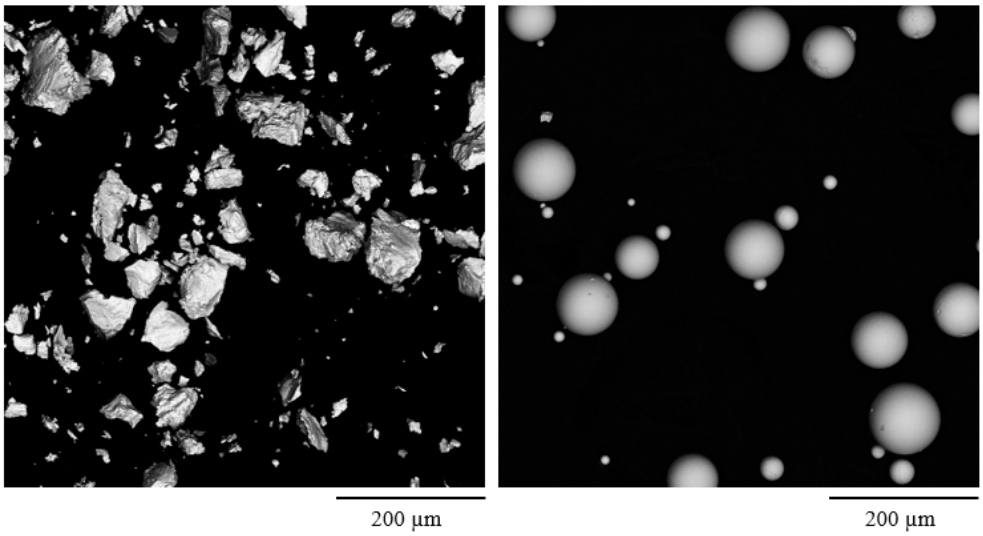

Figure 1: SEM micrographs of starting powder (*left*) and plasma processed powder (*right*). The starting powder had an angular morphology and the plasma processed powder was spherical.

Circularity of the powder was calculated using the area and perimeter data acquired using the ASPEX SEM automated feature analysis. The overall average circularity of the particles increased from 0.56 for the starting powder to 0.94 for the processed powder. Comparisons of the average circularity for specific particle diameters are shown in Figure 2. It was clear that for particle diameters between 5-100µm that the processed powder had higher circularity compared to the starting powder. Several

average circularity values for the processed powder in a particle size range between 30-100µm were approaching 1 meaning they were almost perfectly circular. A decrease in circularity was observed for processed powder particles larger than 100 µm. This drop in circularity was due to agglomeration of the particles.

Table 2: Numeric and volumetric D-values for starting and processed powder. Numeric D-values showed a reduction of fines. Volumetric D90 indicated no significant agglomeration occurred.

		Starting Powder	Tekna Processed
Numeric	D10	1.1	7.6
	D50	6.9	22.9
	D90	37.3	74.5
Volumetric	D10	32.1	49.6
	D50	63.0	76.7
	D90	102.8	100.7

The increase in circularity of the processed powder should lead to an increase in flowability. Two methods were used to determine the flowability of the powder. The first was determination of the Hausner ratio by measuring the apparent and tap densities. The starting powder had apparent and tap densities of 2.88 ± 0.01 g/cc and 3.56 ± 0.05 g/cc respectively. The Hausner ratio was computed by dividing the tap density by the apparent density. The Hausner ratio of the starting powder was 1.23. This value indicates that the powder had fair flow properties [23]. The processed powder had an increase in both apparent and tap densities where the apparent density was 3.83 ± 0.01 g/cc and the tap density was 4.25 ± 0.05 g/cc. The Hausner ratio was therefore decreased to 1.10 which indicated excellent flow properties. Further flowability testing was conducted using a Revolution Flowability Analyzer that consists of a rotating drum where the avalanche

angle was measured. Larger avalanche angles result from an increase in inter-particle forces holding the particles together and is a sign of decreased flow properties. The starting powder had an avalanche angle of 51.4° and the processed powder avalanche angle was 40.4° showing that the processed powder had better flow properties. This result was in agreement with what was determined using the Hausner ratio.

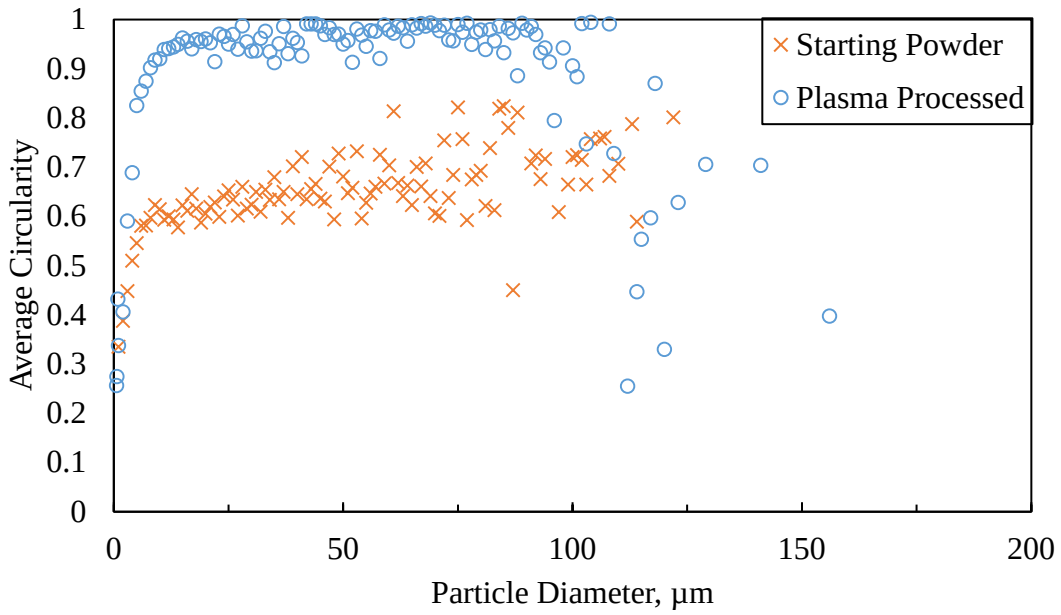

Figure 2: Average circularity as a function of particle diameter for starting and plasma processed powder. The average circularity of the processed powder was higher for most particle diameters.

The overall average chemistry of the particles analyzed using the ASPEX SEM automated feature analysis as well as chemistry for certain particle sizes are shown in Table 3. The starting powder contained an elevated amount of copper compared to the expected alloy composition. On the other hand, the processed powder had a more consistent chemistry. The chemistry distribution was then graphed (see Figure 3) in order

to allow insight into this reduction of copper. It can be seen here that apart from the elevated copper in the starting powder the distribution of chemistry was wider. The fine particles had chemistry that was high in copper and oxygen that spread the distribution. After processing, and consequently the removal of fines, the powder had a tighter distribution of chemistry. The removal of fines did not explain the reduction of copper in the plasma processed powder, as all particle sizes showed elevated copper in the starting powder. Further exploration into the microstructure of the starting powder was necessary to explain the homogenization of the processed powder.

Table 3: Average chemistry in weight percent of both starting and plasma processed powder analyzed using EDS. The plasma processed powder had the chemistry expected for the alloy while the starting powder had elevated amounts of copper.

	Diameter (μm)	Zr	Cu	Ni	Al	Nb	O
Starting Powder	All	50.8	20.6	14.6	4.0	4.5	5.5
	< 25	52.5	18.6	13.2	5.2	4.9	5.6
	< 50	50.7	20.4	14.6	4.0	4.5	5.9
	< 75	50.8	20.3	14.6	4.0	4.5	5.8
	> 75	50.6	21.9	14.6	3.9	4.6	4.4
Plasma Processed	All	64.0	12.7	12.9	3.4	5.2	1.9
	< 25	69.1	10.7	10.2	2.3	5.5	2.2
	< 50	69.7	8.1	11.8	2.4	5.6	2.4
	< 75	67.2	10.0	12.3	3.2	5.4	1.9
	> 75	59.1	16.7	13.7	3.8	4.8	1.8

In order to fully characterize the chemistry of the powder samples, particles were mounted and polished to yield cross-sections to enable chemistry in the bulk of the particle to be determined. The elemental EDS maps for cross-sectioned particles are

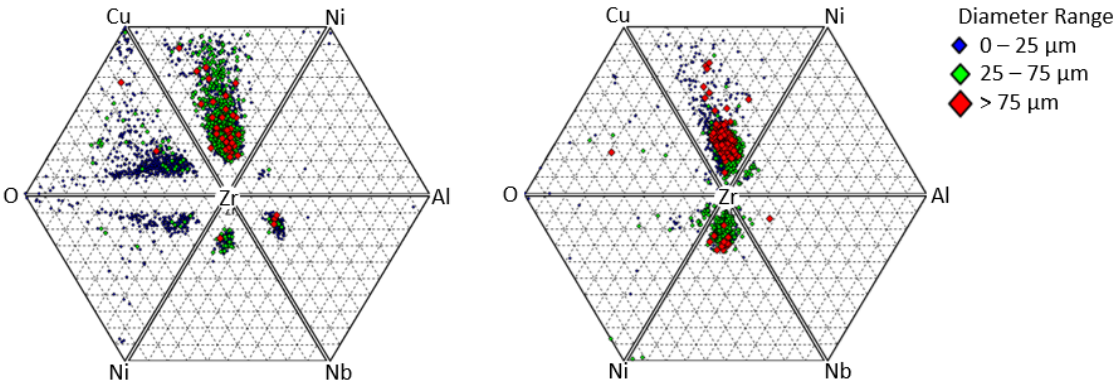

Figure 3: Chemistry of starting powder (*left*) and plasma processed powder (*right*). The reduction of fines in the plasma processed powder tightened the chemistry distribution.

shown in Figure 4. The SEM micrograph of the starting powder microstructure showed needle like structures inside the particle that varied from 7.4-24.7µm in length and 0.8-2.7µm in width. These structures were lean in nickel and high in aluminum, niobium and zirconium. This phase was likely Al_3Nb with dissolved Zr. Studies have shown that ~ 12.5 at. % Zr can be dissolved in Al_3Nb at elevated temperatures [24]. The presence of Al_3Nb is also consistent with the XRD spectra shown in Figure 5. Clustered regions high in copper and zirconium were also observed throughout the particle, which was also consistent with the XRD spectra. The elevated copper found in the starting powder was likely due to the EDS being collected on regions where these copper rich intermetallics were present. Selective vaporization could have played a role as well. In contrast, no phases could be qualitatively noted in the SEM micrographs of the processed powder. These particles had a more homogeneous mixture of elements and no areas of elemental segregation were observed.

XRD was used to determine whether the samples were amorphous and for identification of crystalline phases. The spectra for the starting and processed powder are

shown in Figure 5. Both powder samples had crystalline phases present. The processed sample did have an amorphous hump while the starting powder only had crystalline peaks. It can be concluded that the processing of the powder did result in a reduction of the crystalline phases. XRD indexing indicated that the starting powder sample had a mixture of crystalline phases including Zr, ZrCu, $CuZr_2$, Al_3Nb, $AlNi_3$, and NiO [25–28]. After plasma processing the peaks associated with $AlNi_3$, $CuZr_2$ and NiO were still present.

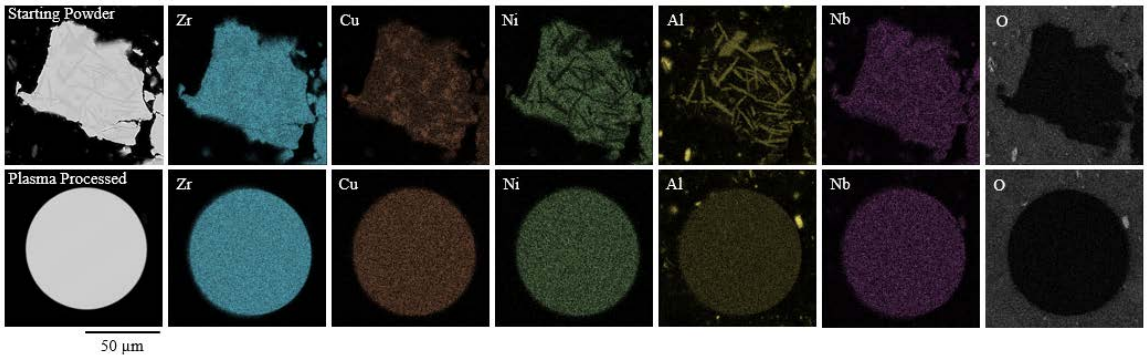

Figure 4: EDS maps of cross-sectioned starting (*top*) and plasma processed (*bottom*) powder. The starting powder sample had elemental segregation where needle-like regions of Al_3Nb with dissolved Zr and clusters of Cu and Zr intermetallics were present.

DSC was used to characterize the glass transition and crystallization temperatures of the powder samples and the results are shown in Figure 6. The starting powder showed no glass transition or crystallization events. The DSC agreed well with the XRD of the starting powder and both indicated the sample was fully crystallized. The processed powder did show glass transition and crystallization events with temperatures of 396°C and 476°C respectively. This result agreed well with work done by other researchers on Vitreloy 106A where the glass transition varied from 395°C – 405°C and crystallization

occurred at 460°C – 490°C [3], [29]. The glass transition being on the lower end of the range given in literature indicates that the cooling rate was relatively low [3]. This was consistent with the partial crystallization observed in the XRD.

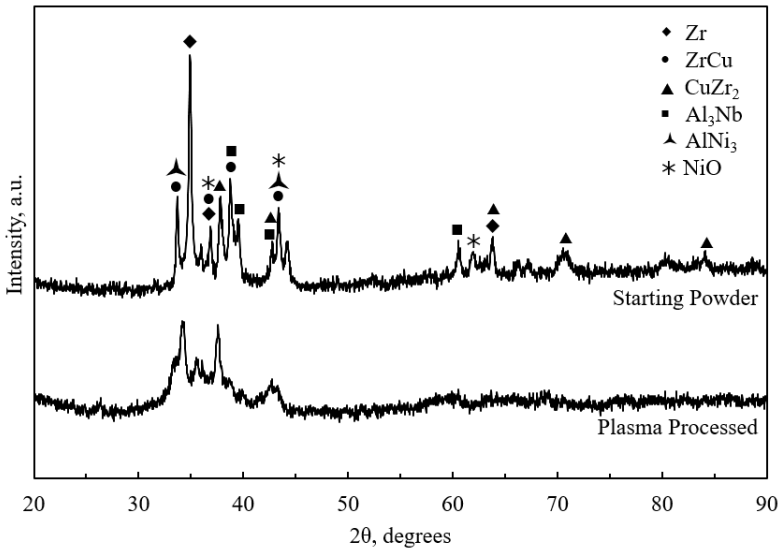

Figure 5: XRD scans of both starting and plasma processed powder with indexed phases shown. The processed powder only had peaks corresponding to $AlNi_3$, $CuZr_2$ and NiO.

Initial observation of metal oxides was made by looking for interference fringe patterns using an optical microscope with a fiber optic light source. Such an oxide can be seen in Figure 7. These oxides were not present on all particles and any oxides found were on the surface of the processed powder particles. Raman spectroscopy was then used for identification of the oxide and the spectra is shown in Figure 7. The peak positions were consistent with those listed for NiO in the literature [28]. This result was surprising as nickel does not form oxides as easily as other elements present in the alloy such as aluminum and zirconium. However, the presence of nickel oxide agrees well with XRD and EDS results. No metal oxides were distinguishable on the surface of the

starting powder because the interference fringe patterns and acquisition of Raman spectroscopy was not possible due to the uneven surface morphology. Oxidation is an important factor to consider when using powders for CS because it can lead to crystallization and porosity [9]. Researchers wanting to use this plasma spheroidization for CS applications may want to take extra precautions such as drying the powder before plasma processing.

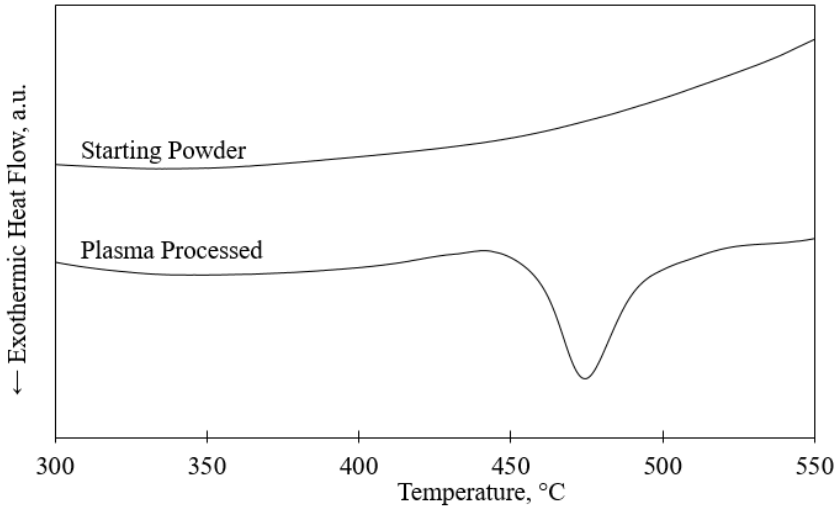

Figure 6: DSC scans of both starting and plasma processed powder. The starting powder was fully crystallized while the plasma processed powder had a glass transition temperature of 396°C and crystallization temperature of 476°C.

In summary, inert ground Vitreloy 106A was processed through and inductively coupled plasma and characterization was completed. With the increase of the sphericity of the powder came an increase of the flowability of the powder from fair to excellent flow properties. Furthermore, homogenization of the chemistry of the powder was accomplished by the removal of fines and the melting and quenching of material. The

powder after processing was also amorphous and had glass transition and crystallization temperatures consistent with literature. Overall, the results of the various characterization techniques used indicated that plasma processing of the inert ground Vitreloy 106A powder had a desirable effect when considering use of the powder for manufacturing techniques such as AM and CS.

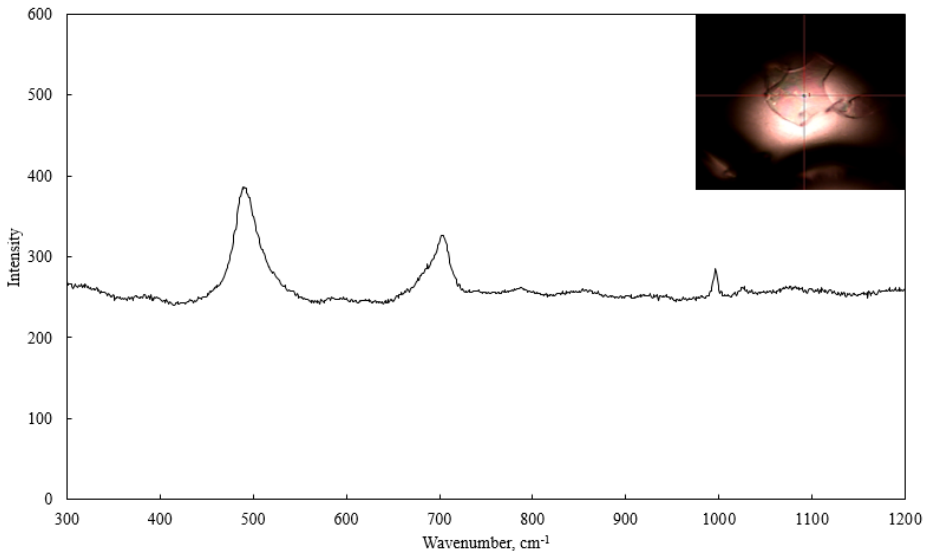

Figure 7: Raman spectra of NiO found on the surface of a plasma processed powder particle. The inset shows the powder particle with the surface oxide with the interference fringe.

4. CONCLUSIONS

Inert ground Vitreloy 106A metallic glass powder was successfully spheroidized using a TekSphero-15 inductively coupled plasma spheroidization system. The material loss to processing, amorphous content, flowability increase, chemistry difference and sphericity were all used to determine whether process parameters were adequate. SEM

micrographs, particle size distributions, and circularity measurements indicated that the processed powder had a high circularity, little agglomeration of particles and a reduction of fines. When comparing the starting and processed powder, the apparent density increased by 33% and the tap density increased by 19%. This resulted in a decrease in the Hausner ratio that indicated improved flowability with processing. This was further confirmed by comparing the avalanche angle, where a decrease was observed for the processed powder. EDS indicated a tightening of the chemistry distribution due to the removal of fines. EDS on cross-sectioned powder samples showed that the starting powder had elemental segregation while the processed powder was homogeneous. Both EDS analysis of cross-sections and XRD were consistent in the identification of intermetallics such as Al_3Nb and CuZr. XRD and DSC corroborated the glassy nature of the processed powder and the thermal transitions captured using DSC were consistent with literature. Raman spectroscopy showed NiO oxides were on the surface on the processed powder. This oxidation could have a detrimental effect to CS coatings, however drying the powder before processing may have a positive effect in the reduction of oxidation. The combination of techniques showed that plasma processing of Vitreloy 106A powder can be used to improve the properties.

ACKNOWLEDGEMENTS

This work was funded by Honeywell Federal Manufacturing & Technologies under Contract No. DE-NA0002839 with the U.S. Department of Energy. The United States Government retains and the publisher, by accepting the article for publication,

acknowledges that the United States Government retains a nonexclusive, paid up, irrevocable, world-wide license to publish or reproduce the published form of this manuscript, or allow others to do so, for the United States Government purposes. The authors would also like to thank Materion for their generous donation of Vitreloy 106A powder, Lyon Davis and Wally Birtch at Tekna for their input and Austin Sutton, Kyle Stagner, Eric Bohannan and Jeff Hill at MS&T for their aid in this research.

REFERENCES

[1] W. H. Wang, C. Dong, and C. H. Shek, “Bulk Metallic Glasses,” *Mater. Sci. Eng. R*, vol. 44, pp. 45–89, 2004.

[2] M. Miller and P. Liaw, Eds., *Bulk Metallic Glasses*. Springer, 2008.

[3] H. Sun and K. M. Flores, “Microstructural Analysis of Laser-Processed Zr-Based Bulk Metallic Glass,” *Metall. Mater. Trans. A*, vol. 41A, pp. 1752–1757, 2010.

[4] A. Gebhardt, “Layer Manufacturing Processes,” in *Understanding Additive Manufacturing*, 2011, pp. 31–63.

[5] Y. Li, Y. Shen, C. Chen, M. C. Leu, and H. L. Tsai, “Building metallic glass structures on crystalline metal substrates by laser-foil-printing additive manufacturing,” *J. Mater. Process. Technol.*, vol. 248, no. May, pp. 249–261, 2017.

[6] Y. Shen, Y. Li, C. Chen, and H. Tsai, “3D printing of large, complex metallic glass structures,” *Mater. Des.*, vol. 117, pp. 213–222, 2017.

[7] X. P. Li, M. P. Roberts, S. O’Keeffe, and T. B. Sercombe, “Selective laser melting of Zr-based bulk metallic glasses: Processing, microstructure and mechanical properties,” *Mater. Des.*, vol. 112, pp. 217–226, 2016.

[8] J. Henao *et al.*, “Deposition mechanisms of metallic glass particles by Cold Gas Spraying,” *Acta Mater.*, vol. 125, pp. 327–339, 2017.

[9] A. Concustell, J. Henao, S. Dosta, N. Cinca, I. G. Cano, and J. M. Guilemany, “On the formation of metallic glass coatings by means of Cold Gas Spray technology,” *J. Alloys Compd.*, vol. 651, pp. 764–772, 2015.

[10] A. T. Sutton, C. S. Kriewall, M. C. Leu, and J. W. Newkirk, “Powder characterisation techniques and effects of powder characteristics on part properties in powder-bed fusion processes,” *Virtual Phys. Prototyp.*, vol. 12, no. 1, pp. 3–29, 2016.

[11] W. Li *et al.*, “Fabrication and characterization of a functionally graded material from Ti-6Al-4V to SS316 by laser metal deposition,” *Addit. Manuf.*, vol. 14, pp. 95–104, 2017.

[12] T. Amine, C. S. Kriewall, and J. W. Newkirk, “Long-Term Effects of Temperature Exposure on SLM 304L Stainless Steel,” *Jom*, vol. 70, no. 3, pp. 384–389, 2018.

[13] S. Yoon, J. Kim, G. Bae, B. Kim, and C. Lee, “Formation of coating and tribological behavior of kinetic sprayed Fe-based bulk metallic glass,” *J. Alloys Compd.*, vol. 509, no. 2, pp. 347–353, 2011.

[14] M. Boulos, “Plasma power can make better powders,” *Met. Powder Rep.*, vol. 59, no. 5, pp. 16–21, 2004.

[15] Y.-L. Li and T. Ishigaki, “Spheroidization of Titanium Carbide Powders by Induction Thermal Plasma Processing,” *J. Am. Ceram. Soc.*, vol. 84, no. 9, pp. 1929–1936, 2004.

[16] L. Ji, C. Wang, W. Wu, C. Tan, G. Wang, and X.-M. Duan, “Spheroidization by Plasma Processing and Characterization of Stainless Steel Powder for 3D Printing,” *Metall. Mater. Trans. A*, vol. 48, no. 10, pp. 4831–4841, 2017.

[17] R. Vert, R. Pontone, R. Dolbec, L. Dionne, and M. I. Boulos, “Induction Plasma Technology Applied to Powder Manufacturing: Example of Titanium-Based Materials,” *Key Eng. Mater.*, vol. 704, pp. 282–286, 2016.

[18] X. L. Jiang and M. Boulos, “Induction plasma spheroidization of tungsten and molybdenum powders,” *Trans. Nonferrous Met. Soc. China (English Ed.*, vol. 16, no. 1, pp. 13–17, 2006.

[19] Z. Evenson, T. Schmitt, M. Nicola, I. Gallino, and R. Busch, “High temperature melt viscosity and fragile to strong transition in Zr–Cu–Ni–Al–Nb(Ti) and Cu47Ti34Zr11Ni8 bulk metallic glasses,” *Acta Mater.*, vol. 60, no. 12, pp. 4712–4719, 2012.

[20] A. S. B212, “Standard Test Method for Apparent Density of Free-Flowing Metal Powders Using the Hall Flowemeter Funnel,” pp. 1–4, 2017.

[21] A. S. B527, “Standard Test Method for Tap Denisty of Metal Powders and Compounds,” pp. 1–4, 2015.

[22] H. H. Hausner, “Friction Conditions in a Mass of Metal Powder.pdf.” International Journal of Powder Metallurgy, pp. 7–13, 1967.

[23] R. L. Carr, “Evaluating Flow Properties of Solids,” *Chem. Eng.*, vol. 72, pp. 163–168, 1965.

[24] G. E. Ilyenko, Ed., “Al-Nb-Zr (Aluminum - Niobium - Zirconium),” in *Light Metal Systems. Part 3*, Berlin: Springer.

[25] Y. Li, Y. Shen, C. Hung, M. C. Leu, and H. Tsai, “Additive manufacturing of Zr-based metallic glass structures on 304 stainless steel substrates via V/Ti/Zr intermediate layers,” *Mater. Sci. Eng. A*, vol. 729, no. January, pp. 185–195, 2018.

[26] R. Vilar, O. Conde, and S. Franco, “Crystallographic structure of Al3Nb in laser-processed Al-Nb alloys,” *Intermetallics*, vol. 7, no. 11, pp. 1227–1233, 1999.

[27] ICDD, *PDF-4+2018 (Database), edited by Dr. Soorya Kabekkodu*. Newtown Square, PA, USA, 2018.

[28] “RRUFF Database.” [Online]. Available: http://rruff.info/chem=Ni,O/display=default/R080121. [Accessed: 02-Oct-2018].

[29] I. Karaman, J. Robertson, J. T. Im, S. N. Mathaudhu, Z. P. Luo, and K. T. Hartwig, “The Effect of Temperature and Extrusion Speed on the Consolidation of Zirconium-Based Metallic Glass Powder Using Equal-Channel Angular Extrusion,” *Metall. Mater. Trans. A Phys. Metall. Mater. Sci.*, vol. 35 A, no. 1, pp. 247–256, 2004.

SECTION

3. SUMMARY, CONCLUSIONS AND RECOMMENDATIONS FOR FUTURE WORK

This research aimed at using powder characterization methods to provide insight into powder usage in the SLM process and differences attained during tailoring via spheroidization process. A study incorporating different builds and argon gas cross-flow rates in the SLM processing of 304L SS was first used to build parts under non-ideal conditions. Powder collected from inside the build area was then used to determine that SEM micrographs, particle size distributions, and XRD measurements were the best ways to detect heat-affected powder. The conditions where heat-affected powder was deposited and detected in the build area correlated to a decrease in yield strength and ultimate tensile strength with an increase in porosity and surface roughness.

The knowledge of suitable powder characterization methods was then used to develop a methodology to design a recycling study of 304L SS. The amount of heat-affected powder generated during a build was directly related to the amount of time the laser was interacting with the powder bed. Therefore, exploration of different area fractions was necessary as the heat-affected powder should have an effect on powder degradation. In this research, 7 builds consisting of different area fractions and part spacings were completed through 3 iterations. After each iteration powder was tested by determining particle size distributions, computing the Hausner ratio and quantifying phases using XRD. All of these methods were able to detect differences in the powder with XRD showing the clearest distinction. The part properties were determined and were

consistent for 3 iterations of all builds tested. In order to have a recycling study where powder degradation is observed (serving as a worst case study), ≥ 25% of the build area needs to be utilized for a 304L SS powder recycling study via SLM.

Powder characterization methods were also used to assess the success of plasma spheroidization to tailor Vitreloy 106A inert ground powder. The morphology of the inert ground powder was angular and not suitable for use in the SLM process. A TekSphero-15 was used for plasma processing to improve powder properties. The plasma processed powder had little agglomeration as evidenced by the SEM micrographs, particle size distributions and average circularity measurements. The overall circularity of the powder increased from 0.56 for the starting powder to 0.94 for the plasma processed powder. This increase in circularity resulted in a decrease in Hausner ratio indicating that the plasma processed powder has better flow properties than the starting powder. XRD and DSC confirmed that the plasma processed powder was amorphous with partial crystallization while the starting powder was fully crystallized. Raman spectroscopy was used to determine that NiO oxides were on the surface of the processed powder. Overall, the plasma processing was deemed successful and had a positive effect on the powder properties.

Recommendations for future work include:

- A more in depth recycling study on SLM of 304L SS spanning several iterations with at least 25% area fraction of the build populated with parts. This recycling study should focus on comprehensive powder and part characterization for each iteration of builds.

- Use the spheroidized Vitreloy 106A bulk metallic glass powder to optimize build parameters in SLM
    - Compare the part properties of spheroidized powder and staring powder, gas-atomized powder, crystalline powder
- Spheroidize the large size fraction (+88μm) of Vitreloy 106A powder and use this for blown powder-based AM depositions
    - Compare part properties of powder bed vs blown powder-based AM

BIBLIOGRAPHY

[1] W. D. Callister, *Materials Science and Engineering An Introduction*, 7th Editio. New York: John Wiley & Sons, Inc., 2007.

[2] J. Stodart Esq. and M. Faraday, “Experiments on the alloys of steel, made with a view to its improvement,” *Philos. Mag.*, vol. 56, no. 267, pp. 26–35, 1820.

[3] H. M. Cobb, *The History of Stainless Steel*. Materials Park, OH: ASM International, 2010.

[4] P. Monnartz, “The study of iron-chromium alloys withe special consideration of their resistance to acids,” *Metallurgie*, 1911.

[5] D. A. Jones, “Passivity,” in *Principles and Prevention of Corrosion*, 2nd Editio., 1996, pp. 116–142.

[6] C. C. Silva, J. P. Farias, and H. B. de Sant’Ana, “Evaluation of AISI 316L stainless steel welded plates in heavy petroleum environment,” *Mater. Des.*, vol. 30, no. 5, pp. 1581–1587, 2009.

[7] A. Saha Podder and A. Bhanja, “Applications of Stainless Steel in Automobile Industry,” *Adv. Mater. Res.*, vol. 794, pp. 731–740, 2013.

[8] N. R. Baddoo, “Stainless steel in construction: A review of research, applications, challenges and opportunities,” *J. Constr. Steel Res.*, vol. 64, no. 11, pp. 1199–1206, 2008.

[9] C. Lelièvre, P. Legentilhomme, C. Gaucher, J. Legrand, C. Faille, and T. Bénézech, “Cleaning in place: Effect of local wall shear stress variation on bacterial removal from stainless steel equipment,” *Chem. Eng. Sci.*, vol. 57, no. 8, pp. 1287–1297, 2002.

[10] C. O. A. Olsson and D. Landolt, “Passive films on stainless steels - Chemistry, structure and growth,” *Electrochim. Acta*, vol. 48, no. 9 SPEC., pp. 1093–1104, 2003.

[11] A. L. Schaeffler, “Constitution diagram for stainless steel weld metal,” *Met. Prog.*, vol. 56, no. 11, p. 680–680B, 1949.

[12] D. J. Kotecki and T. A. Siewert, “WRC-1992 Constitution Diagram for Stainless Steel Weld Metals : A Modification of the WRC-1988 Diagram,” *AWS Annu. Meet.*, pp. 171–178, 1992.

[13] D. J. Kotecki, “Verification of the NBS-CSM ferrite diagram,” in *International Institute of Welding*, 1988.

[14] P. Korinko and S. Malene, “Considerations for the weldability of types 304L and 316L stainless steel,” *J. Fail. Anal. Prev.*, vol. 1, no. 4, pp. 61–68, 2001.

[15] A.-17 A. Standards, *Standard Specification for Chromium and Chromium-Nickel Stainless Steel Plate , Sheet , and Strip for Pressure Vessels and for General Applications*. 2017.

[16] J. F. Löffler, “Bulk metallic glasses,” *Intermetallics*, vol. 11, no. 6, pp. 529–540, 2003.

[17] M. Miller and P. Liaw, Eds., *Bulk Metallic Glasses*. Springer, 2008.

[18] A. Inoue, “Bulk amorphous and nanocrystalline alloys with high functional properties,” *Mater. Sci. Eng. A*, vol. 304–306, no. 1–2, pp. 1–10, 2001.

[19] W. Klement, R. H. Willens, and P. Duwez, “Non-crystalline structure in solidified gold–silicon alloys,” 1960.

[20] W. H. Wang, C. Dong, and C. H. Shek, “Bulk Metallic Glasses,” *Mater. Sci. Eng. R*, vol. 44, pp. 45–89, 2004.

[21] H. R. Sistla and D. J. Newkirk, “Microstructural and mechanical characterization of laser deposited advanced materials,” 2014.

[22] C. Suryanarayana and A. Inoue, *Bulk Metallic Glasses*. 2011.

[23] J. Schroers, “Processing of bulk metallic glass,” *Adv. Mater.*, vol. 22, no. 14, pp. 1566–1597, 2010.

[24] H. Sun and K. M. Flores, “Microstructural Analysis of Laser-Processed Zr-Based Bulk Metallic Glass,” *Metall. Mater. Trans. A*, vol. 41A, pp. 1752–1757, 2010.

[25] X. P. Li, M. P. Roberts, S. O’Keeffe, and T. B. Sercombe, “Selective laser melting of Zr-based bulk metallic glasses: Processing, microstructure and mechanical properties,” *Mater. Des.*, vol. 112, pp. 217–226, 2016.

[26] Y. Li, Y. Shen, C. Hung, M. C. Leu, and H. Tsai, “Additive manufacturing of Zr-based metallic glass structures on 304 stainless steel substrates via V/Ti/Zr intermediate layers,” *Mater. Sci. Eng. A*, vol. 729, no. January, pp. 185–195, 2018.

[27] Y. Li, Y. Shen, C. Chen, M. C. Leu, and H.-L. Tsai, “Building metallic glass structures on crystalline metal substrates by laser-foil-printing additive manufacturing,” *J. Mater. Process. Technol.*, vol. 248, pp. 249–261, Oct. 2017.

[28] Z. Evenson, S. Raedersdorf, I. Gallino, and R. Busch, “Equilibrium viscosity of Zr-Cu-Ni-Al-Nb bulk metallic glasses,” *Scr. Mater.*, vol. 63, pp. 573–576, 2010.

[29] I. Gibson, D. Rose, and B. Stucker, *Additive Manufacturing Technologies*, 2nd Editio. New York, 2015.

[30] Y. Zhai, D. A. Lados, and J. L. Lagoy, “Additive Manufacturing: Making imagination the major Limitation,” *JOM*, vol. 66, no. 5, pp. 808–816, 2014.

[31] P. K. Samal and J. W. Newkirk, “Powder Metallurgy, Metal Powder Characterization, Bulk Properties of Powders,” *ASM Handb.*, vol. 7, pp. 93–168, 2015.

[32] A. Gebhardt, “Layer Manufacturing Processes,” in *Understanding Additive Manufacturing*, 2011, pp. 31–63.

[33] K. Guan, Z. Wang, M. Gao, X. Li, and X. Zeng, “Effects of processing parameters on tensile properties of selective laser melted 304 stainless steel,” *Mater. Des.*, vol. 50, pp. 581–586, 2013.

[34] R. M. Mahamood, E. T. Akinlabi, M. Shukla, and S. Pityana, “Revolutionary Additive Manufacturing: An Overview.,” *Lasers Eng. (Old City Publ.*, vol. 27, no. 3/4, pp. 161–178, 2014.

[35] M. Simonelli *et al.*, “A Study on the Laser Spatter and the Oxidation Reactions During Selective Laser Melting of 316L Stainless Steel, Al-Si10-Mg, and Ti-6Al-4V,” *Metall. Mater. Trans. A*, 2015.

[36] M. J. Zhang, G. Y. Chen, Y. Zhou, S. C. Li, and H. Deng, “Observation of spatter formation mechanisms in high-power fiber laser welding of thick plate,” *Appl. Surf. Sci.*, vol. 280, pp. 868–875, 2013.

[37] Y. Liu, Y. Yang, S. Mai, D. Wang, and C. Song, “Investigation into spatter behavior during selective laser melting of AISI 316L stainless steel powder,” *Mater. Des.*, vol. 87, pp. 797–806, 2015.

[38] A. T. Sutton, C. S. Kriewall, M. C. Leu, and J. W. Newkirk, “Characterization of Heat-Affected Powder Generated during the Selective Laser Melting of 304L Stainless Steel Powder,” in *Proceedings from the 27th Annual International Solid Freeform Fabrication Symposium*, 2017, pp. 261–276.

[39] A. Ladewig, G. Schlick, M. Fisser, V. Schulze, and U. Glatzel, “Influence of the shielding gas flow on the removal of process by-products in the selective laser melting process,” *Addit. Manuf.*, vol. 10, pp. 1–9, 2016.

[40] B. Ferrar, L. Mullen, E. Jones, R. Stamp, and C. J. Sutcliffe, “Gas flow effects on selective laser melting (SLM) manufacturing performance,” *J. Mater. Process. Technol.*, vol. 212, no. 2, pp. 355–364, 2012.

[41] P. Shcheglov, S. Gumenyuk, I. Gornushkin, M. Rethmeier, and V. Petrovskiy, “Vapor–plasma plume investigation during high-power fiber laser welding,” *Laser Phys.*, vol. 23, no. 1, 2013.

[42] M. Barclift, S. Joshi, T. Simpson, and C. Dickman, “Cost modeling and depreciation for reused powder feedstock in powder bed fusion additive manufacturing,” *Solid Free. Fabr. Symp.*, pp. 2007–2028, 2016.

[43] H. P. Tang, M. Qian, N. Liu, X. Z. Zhang, G. Y. Yang, and J. Wang, “Effect of Powder Reuse Times on Additive Manufacturing of Ti-6Al-4V by Selective Electron Beam Melting,” *Jom*, vol. 67, no. 3, pp. 555–563, 2015.

[44] L. C. Ardila *et al.*, “Effect of IN718 Recycled Powder Reuse on Properties of Parts Manufactured by Means of Selective Laser Melting,” *Phys. Procedia*, vol. 56, pp. 99–107, 2014.

[45] J. A. Slotwinski, E. J. Garboczi, P. E. Stutzman, C. F. Ferraris, S. S. Watson, and M. A. Peltz, “Characterization of metal powders used for additive manufacturing,” *J. Res. Natl. Inst. Stand. Technol.*, vol. 119, pp. 460–493, 2014.

[46] R. J. Goldston and P. H. Rutherford, “Introduction to plasmas,” in *Introduction to Plasma Physircs*, New York, NY: Taylor & Francis, 2000, pp. 1–14.

[47] D. P. Stern, “The Exploration of the Magnetosphere - Plasma,” *NASA*, 2001. [Online]. Available: https://www-spof.gsfc.nasa.gov/Education/wplasma.html. [Accessed: 08-Oct-2018].

[48] D. A. (Stanford U. Skoog, J. F. (University of K. Holler, and S. R. (Michigan S. U. Crouch, *Principles of Instrumental Analysis*, 6th ed. Thomson Brooks/Cole, 2007.

[49] M. Murillo and J. M. Mermet, “Improvement of the energy transfer with added-hydrogen in inductively coupled plasma atomic emission spectroscopy,” *Spectrochim. Acta Part B At. Spectrosc.*, vol. 44, no. 4, pp. 359–366, 1989.

[50] R. H. Scott, V. A. Fassel, R. N. Kniseley, and D. E. Nixon, “Inductively Coupled Plasma-Optical Emission Analytical Spectrometry: A Compact Facility for Trace Analysis of Solutions,” *Anal. Chem.*, vol. 46, no. 1, pp. 75–80, 1974.

[51] P. Baedecker, “Methods for geochemical analysis,” *USGS Bull.*, vol. 1770, pp. 33, 34, 1987.

[52] V. A. Fassel and R. N. Kniseley, “Inductively Coupled Plasma-Optical Emission Spectroscopy,” *Anal. Chem.*, vol. 46, no. 13, p. 1110A–1120A, 1974.

[53] U. Schaltegger, A. K. Schmitt, and M. S. A. Horstwood, “U-Th-Pb zircon geochronology by ID-TIMS, SIMS, and laser ablation ICP-MS: Recipes, interpretations, and opportunities,” *Chem. Geol.*, vol. 402, pp. 89–110, 2015.

[54] S. E. Jackson, N. J. Pearson, W. L. Griffin, and E. A. Belousova, “The application of laser ablation-inductively coupled plasma-mass spectrometry to in situ U-Pb zircon geochronology,” *Chem. Geol.*, vol. 211, no. 1–2, pp. 47–69, 2004.

[55] D. M. Chew, J. A. Petrus, and B. S. Kamber, “U-Pb LA-ICPMS dating using accessory mineral standards with variable common Pb,” *Chem. Geol.*, vol. 363, pp. 185–199, 2014.

[56] M. Boulos, “Plasma power can make better powders,” *Met. Powder Rep.*, vol. 59, no. 5, pp. 16–21, 2004.

[57] “TekSphero Spheroidization Systems,” *Tekna*. [Online]. Available: http://www.tekna.com/spheroidization-systems. [Accessed: 08-Oct-2018].

[58] L. Ji, C. Wang, W. Wu, C. Tan, G. Wang, and X.-M. Duan, “Spheroidization by Plasma Processing and Characterization of Stainless Steel Powder for 3D Printing,” *Metall. Mater. Trans. A*, vol. 48, no. 10, pp. 4831–4841, 2017.

[59] R. Vert, R. Pontone, R. Dolbec, L. Dionne, and M. I. Boulos, “Induction Plasma Technology Applied to Powder Manufacturing: Example of Titanium-Based Materials,” *Key Eng. Mater.*, vol. 704, pp. 282–286, 2016.

[60] Y.-L. Li and T. Ishigaki, “Spheroidization of Titanium Carbide Powders by Induction Thermal Plasma Processing,” *J. Am. Ceram. Soc.*, vol. 84, no. 9, pp. 1929–1936, 2004.

[61] X. L. Jiang and M. Boulos, “Induction plasma spheroidization of tungsten and molybdenum powders,” *Trans. Nonferrous Met. Soc. China (English Ed.*, vol. 16, no. 1, pp. 13–17, 2006.

[62] Z. Evenson, T. Schmitt, M. Nicola, I. Gallino, and R. Busch, “High temperature melt viscosity and fragile to strong transition in Zr–Cu–Ni–Al–Nb(Ti) and Cu47Ti34Zr11Ni8 bulk metallic glasses,” *Acta Mater.*, vol. 60, no. 12, pp. 4712–4719, 2012.

VITA

Caitlin Shea Kriewall was born in Edmond, Oklahoma on August 5, 1992. She graduated from Sequoyah High School in Claremore, Oklahoma in May 2010. She then went to the University of Central Oklahoma in Edmond, Oklahoma to pursue a bachelor's degree in Chemistry with a minor in mathematics. She graduated cum laude in May 2014. She received her Master's in Materials Science and Engineering from Missouri University of Science and Technology in Rolla, Missouri in December 2018. She was a member of Alpha Sigma Mu, the professional honor society for materials science and engineering.